Applied Acoustics

Application of Spectral Kurtosis on vibration signals for the detection of cavitation in centrifugal pumps

--Manuscript Draft--

Manuscript Number:	
Article Type:	Research Paper
Section/Category:	Europe and Rest of the World
Keywords:	centrifugal pumps; condition monitoring; cavitation detection; flow visualisation; Spectral Kurtosis; vibration measurements
Corresponding Author:	Georgios Mousmoulis, PhD National Technical University of Athens Athens, Please select ... GREECE
First Author:	Georgios Mousmoulis, PhD
Order of Authors:	Georgios Mousmoulis, PhD
	Christos Yiakopoulos, PhD
	George Aggidis, PhD
	Ioannis Antoniadis, PhD
	Ioannis Anagnostopoulos, PhD
Abstract:	The detection of cavitation formation in hydraulic turbomachinery has been widely investigated due to its significant impact on their steady and dynamic operation. The aim of this study is the application of Spectral Kurtosis tool in order to effectively detect the impulsive shock waves generated during the implosion of vapour bubbles. The methodology is applied and evaluated on the vibration signals obtained from two different semi-open impellers. The effects of loading conditions, along with the different geometrical characteristics of each impeller are examined. The test rig is manufactured from Plexiglas parts in order to be able to visualise and verify the presence of cavities in the rotating impeller. The results under initial cavitating conditions show that the high frequency implosions of vapour bubbles interact with the low frequency passing of the rotating blades and compose part of the vibration signal. The application of the band pass filter, with central frequency and bandwidth estimated from the Fast Kurtogram, to the original signal allows to extract this information both in time and in frequency domain, and to correlate the periodic impulsive behaviour with the blade passing frequency of the impeller. The present results support the establishment of a robust detection cavitation criterion in centrifugal pumps and show that Spectral Kurtosis is a useful tool for the prevention of related faults in centrifugal pumps.
Suggested Reviewers:	Konstantinos Gryllias, PhD Associate Professor, KU Leuven: Katholieke Universiteit Leuven konstantinos.gryllias@kuleuven.be Expert in: *Signal Processing *Fault detection/diagnosis/prognosis of rotating machinery and structures *Condition monitoring *Pattern recognition & Classification methods
	Nicole Kessissoglou, PhD Professor, UNSW: University of New South Wales n.kessissoglou@unsw.edu.au Expert in: *Structural vibration and transmission *Fluid-structure interaction *Active noise and vibration control
	David Mba, PhD Professor, De Montfort University david.mba@dmu.ac.uk

	Expert in: *machine condition monitoring *machine fault diagnosis *machine performance prediction
	Jérôme Antoni, PhD Professor, INSA Lyon: Institut National des Sciences Appliquees de Lyon jerome.antoni@insa-lyon.fr Expert in: *Structural Vibration *Vibration Analysis *Structural Health Monitoring *Vibration Testing *Condition Monitoring
	Xavier Escaler, PhD Lecturer, Universitat Politècnica de Catalunya: Universitat Politecnica de Catalunya escaler@mf.upc.edu Expert in: *cavitating flows *fluid-structure interaction *dynamic behaviour of rotating machinery
Opposed Reviewers:	

To the Editors of the Journal of Applied Acoustics:

Please consider the attached manuscript entitled “Application of Spectral Kurtosis on vibration signals for the detection of cavitation in centrifugal pumps” for possible publication in the Journal of Applied Acoustics.

The paper applies spectral kurtosis tool in order to detect early stage cavitation development in centrifugal pumps. The methodology is applied and evaluated on the vibration signals obtained from two different impellers in a laboratory test rig, where the casing of the pump was made from Plexiglas parts in order to visualise two-phase flow formation in the rotating impeller. The results obtained from both impellers tested, show that the application spectral kurtosis tool related cavitation with the appearance of BPF at the envelope spectrum of the filtered signal as well as with the impulsive behavior at the filtered time series. The paper results support the definition of a robust detection cavitation criterion and make the spectral kurtosis a useful tool for the prevention of related faults in centrifugal pumps.

Please let us know if this submittal meets your requirements for sending in manuscripts for possible review, and please feel free to contact us for anything else you may require.

Thank you for possibly considering this manuscript,

Dr. Georgios Mousmoulis
National Technical University of Athens
Heroon Polytechniou 9, Zografou, Athens, 15780, Greece
E-mail: mousmoulisgeorge@mail.ntua.gr

Application of Spectral Kurtosis on vibration signals for the detection of cavitation in centrifugal pumps

G. Mousmoulis[1,*], C. Yiakopoulos[2], G. Aggidis[3], I. Antoniadis[2], I. Anagnostopoulos[1]

[1]Laboratory of Hydraulic Turbomachines, School of Mechanical Engineering, National Technical University of Athens, Iroon Polytechniou 9, Zografou, Athens, 15780, Greece

[2]Laboratory of Dynamics and Structures, School of Mechanical Engineering, National Technical University of Athens, Iroon Polytechniou 9, Zografou, Athens, 15780, Greece

[3]Lancaster University Renewable Energy Group, Department of Engineering, Lancaster University, Bailrigg, Lancaster, LA1 4YW, United Kingdom,

E-mail addresses:

mousmoulisgeorge@mail.ntua.gr (*Corresponding author, Dr. Georgios Mousmoulis)

chryiako@central.ntua.gr (Dr. Christos Yiakopoulos)

g.aggidis@lancaster.ac.uk (Pr. George Aggidis)

antogian@central.ntua.gr (Pr. Ioannis Antoniadis)

anagno@fluid.mech.ntua.gr (Pr. Ioannis Anagnostopoulos)

Abstract

The detection of cavitation formation in hydraulic turbomachinery has been widely investigated due to its significant impact on their steady and dynamic operation. The aim of this study is the application of Spectral Kurtosis tool in order to effectively detect the impulsive shock waves generated during the implosion of vapour bubbles. The methodology is applied and evaluated on the vibration signals obtained from two different semi-open impellers. The effects of loading conditions, along with the different geometrical characteristics of each impeller are examined. The test rig is manufactured from Plexiglas parts in order to be able to visualise and verify the presence of cavities in the rotating impeller. The results under initial cavitating conditions show that the high frequency implosions of vapour bubbles interact with the low frequency passing of the rotating blades and compose part of the vibration signal. The application of the band pass filter, with central frequency and bandwidth estimated from the Fast Kurtogram, to the original signal allows to extract this information both in time and in frequency domain, and to correlate the periodic impulsive behaviour with the blade passing frequency of the impeller. The present results support the establishment of a robust detection cavitation criterion in centrifugal pumps and show that Spectral Kurtosis is a useful tool for the prevention of related faults in centrifugal pumps.

Keywords: centrifugal pumps; condition monitoring; cavitation detection; flow visualisation; Spectral Kurtosis; vibration measurements

1. Introduction

The phenomenon of vaporization of liquids at macroscopically isothermal conditions due to decrease of static pressure below vapour pressure value is called cavitation. Centrifugal pumps are machines that convert mechanical to hydraulic power with the use of a rotating impeller with hydrodynamically-shaped blades. The acceleration of the flow and the low pressure conditions prevailing at the entrance of the rotating impeller can create such local conditions that favour the formation of vapour cavities [1]. The area covered by the two-phase flow can modify the hydrodynamic shape of the blades and create flow recirculation and separation regions that eventually decrease the performance and hydraulic efficiency of the pump [2]. In addition, the vapour cavities are shifted downstream by the flow towards higher pressure areas, where they are instantly imploded, creating high energy micro jets and impulsive pressure waves that stress and erode the adjacent metallic surfaces [3]. High levels of noise and vibration can be created if the phenomenon is intense and extensive in the impeller. The aforementioned unwanted impacts on the performance of centrifugal pumps has led researchers and engineers to try to develop techniques for early cavitation detection.

The first method used for the detection of two-phase flow formations in centrifugal pumps, proposes the monitoring of the total head of the machine and identifies cavitation when the latter drops more than 3% [4, 5]. This drop is due to the development of vapour formations in the impeller that cover a substantial part of the flow path and start to block the flow, thus reducing the capability of the impeller to transfer power to the working medium [6-9]. The main advantage of this technique constitutes a general detection cavitation criterion, since the head drop is a common symptom of cavitation presence in all types of centrifugal pumps. While the 3% drop can be identified in the laboratory using relatively low cost and precision measuring devices.

However, application of this method in real operating conditions is not the most efficient approach to detect vapour phased formations, because cavitation even at earlier stages, before the total head drop, can cause significant wear of the impeller surfaces, as also noise and vibration [1-4, 10]. As a consequence, additional tools have been developed for the monitoring of hydraulic turbomachines to identify cavitation presence, based on noise and vibration measurements [7, 9, 11-39]. Signal processing tools are then applied to discern and detect the sound and the mechanical oscillations generated during the implosion of vapour cavities. There are two main challenges in the application of these tools; i) the extraction of cavitation characteristics from the measured signal that are usually masked by the noise and the vibrations of the pump and its motor, and ii) the utilisation of these characteristics towards the formation of a general detection criterion that would be independent from the individual structural and operational features of each installation.

The most common signal processing technique in the literature that has been applied on the noise and vibration signals, deals with the use of the Fourier Transformation or with the calculation of Power Spectral Density (PSD), in order to study the frequency spectrum (FS) of the measured data. The collapse and implosion of the vapour bubbles result in shock pressure waves that excite a wide range of frequencies and make discernible the development of the phenomenon in the spectrum [9, 11-20]. In order to quantify these excitations, some authors calculate the power content in different bands of the spectrum and plot the results as function of cavitation development [4, 11, 14, 18-34]. Interestingly, the majority of the published works notice an increase of the noise and vibration power content in these signals close to the visual inception of the phenomenon, and show that this approach can be used towards the prompt detection of cavitation before total head collapse.

On the other hand, however, the application of the above signal processing method in several different pumps and test configurations, reveals its weakness to provide a safe cavitation detection tool with general applicability. More specifically, comparison of the noise and vibration spectra in various cases shows the excitation of different frequencies from cavitation development [9, 11-20]. Such behaviour highlights the increased randomness of the phenomenon itself, as well as the additional randomness introduced by the interaction of the bubble implosion with the structural and operational characteristics of the machine and the configuration. Hence it is not possible to define a common frequency band in all cases, at which the integration of the noise and vibration power could be used as a general method for prompt detection of cavitation in hydraulic turbomachines.

A second limitation of this detection approach is that the increase of noise and vibration under cavitating conditions requires the knowledge of the level of noise and vibration in the same frequency ranges when the machine operates under healthy, non-cavitating conditions. This information can be obtained during controlled laboratory measurements or for pumps equipped with predictive maintenance monitoring equipment, but not for the vast majority of hydraulic turbomachines in operation.

One additional difficulty and limitation of the above method arises from the use of rolling element bearings that are found to excite wide range of frequencies when operate under faulty conditions, in a similar manner with cavitation phenomenon [40-46]. These similarities in the FS are due to the impulsive behaviour that both these mechanisms exhibit. As a result, additional characteristic have to be found in the measured signal so as to discern the faults related to rolling element bearings from cavitation.

The extraction of the above conclusions from the literature reveals the additional effort towards the formation of a well-rounded cavitation detection criterion that will not change in different machines, as well as it will allow the differentiation of the various impulsive fault mechanism. In addition, the random impulsive noise sources, generated by cavitation bubbles collapse in the pump, cause complex modulation effects. Thus, the vibratory response of a pump

under cavitation is not periodic, but it inherently exhibits cyclic stationary characteristics, as it is generated by a hidden periodic mechanism due to the rotation of shaft and impellers. This means that the statistical moments of the pump response vary periodically with time. When cavitation occurs, the cyclic components begin to be covered by the cavitation impulsive noise. To overcome these difficulties and reveal the cyclic frequencies of the amplitude modulation mechanism, the carrier signals caused by the flow in the impeller and the strong random impulsive interference should be removed from the measurements.

Towards this direction, the application of wavelet analysis has been proposed with the use of microphones [35] and accelerometers [36, 37], where the original signal is decomposed to a number of levels in order to bring out cavitation signal in time. In addition, Sun et al. [38] applied cyclic spectral analysis on the vibration signal and concluded that the onset and development of cavitation is correlated with the quadruple of the Rotational Frequency (RF) of the pump motor. Moreover, the study of the signal's envelope in frequency domain has been proposed by some authors [19, 33 & 39], in order to examine the possible modulation of the frequencies excited by cavitation noise and vibration. In the present study, the frequency spectrum of the envelope is referred for brevity as envelope spectrum (ES). These studies focus on cavitation formations in the runner and the draft tube of Francis turbines, and manage to associate cavitation with discrete low frequency components of the ES. With this approach it is possible to extract the detection information needed to form a common criterion. However, the aforementioned studies do not provide a tool that identifies the frequency band that is used for the signal's demodulation, and as previously discussed, their results deviate significantly among the different testing configurations.

In order to efficiently define the characteristics of the band pass filter used to unmask cavitation noise and vibration, as well as to efficiently extract cavitation information from cyclic frequencies and resonant frequency fields, the present study proposes the use of the Spectral Kurtosis tool (SKT) [47, 48]. The SKT is implemented here for the first time in vibration measurements for the detection of two-phase flow formations in centrifugal pumps. More specifically, two accelerometers are located on the casing of a radial flow centrifugal pump and the cavitation characteristic curves are derived in order to check the capabilities of the proposed detection methodology. The tested pump uses two semi open impellers with different blade geometrical characteristics, so as to investigate their effect on the applicability of the methodology. The pump casing is made of Plexiglas and hence the presence and the extent of vapour formations in the pump can be visualized. The present study justifies the selection of SKT after careful examining the transient behaviour of the statistical moments, as well as the FS in the measured data and highlights the effect of cavitation on the vibration time series (TS) pattern, as well as on the ES under different suction conditions.

The description of the experimental set up and testing procedure is presented at first (section 2), and the mathematical formulation of the detection methodology follows (section 3). Then,

the cavitation test results (section 4) and the appropriate processing of the vibration signals (section 5) are analyzed and discussed, in order to identify the effect of cavitation on the vibration signal, to justify the selection and to evaluate the detection capabilities of the proposed method.

2. Experimental set up

2.1 The pump test laboratory

The test configuration (Fig. 1) is installed in the Engineering Department of Lancaster University. UK, and includes the radial centrifugal pump (i), the main tank (vii), the valves (vi, viii), and the installed sensors for measuring the vibration (ii, iii) and the pump performance (iv, v, ix). A stroboscope (xi) enables to visualise the development of vapour bubbles in the pump. The pump is driven by an induction motor with 3 horsepower rated output at constant rotational speed, n=1800 rpm, while the water temperature during the test was T=23 ºC.

Figure 1 highlights the main advantage of this test rig for the study and visual inspection of cavitation inception and development; the volute, the front casing of the pump and all the piping system are made from Plexiglas material. In this way it is possible to visualise the flow cavitating conditions in the pump impeller and the suction pipe system. In addition, the pump does not have its own bearings but all the mechanical and hydraulic loads are transferred to the bearings of the motor. This facilitates the detection of cavitation phenomenon, since the noise and vibration emitted from the bearings is more difficult to surpass the cavitation noise and vibration in the impeller.

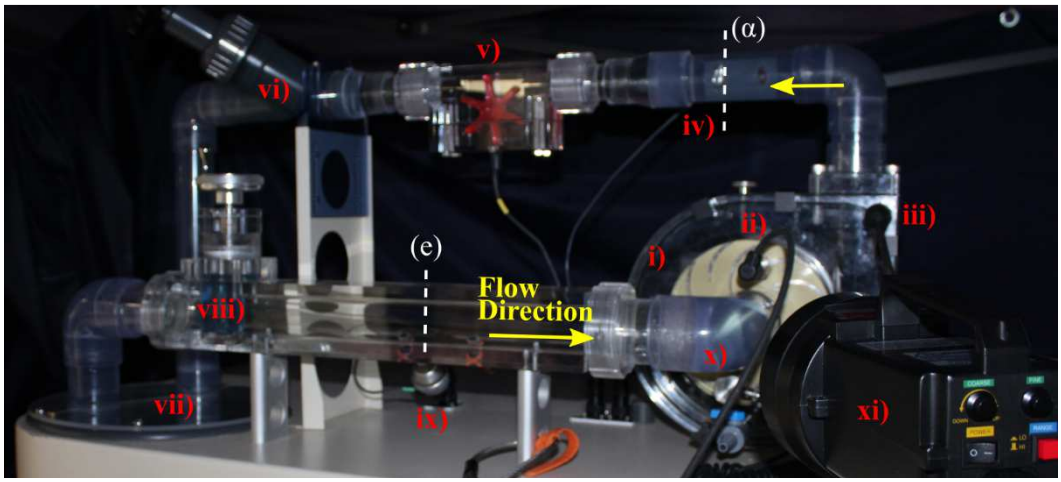

Fig. 1. Laboratory test rig configuration; i) pump, ii) accelerometer B01, iii) accelerometer A01, iv) discharge pressure transducer, v) flow meter, vi) discharge valve, vii) water tank, viii) suction valve, ix) suction pressure transducer, x) 90º elbow, xi) stroboscope.

The tests include the investigation of two impellers with different geometric design, one with curved main and splitter blades (impeller No. 1, Fig. 2a) and a second with straight, radial blades (impeller No. 2, Fig. 2b). Both are unshrouded, semi-open impellers, made from aluminum, and their geometrical characteristics are given in Table 1, where R is the radius (Fig. 2a,c), β the blade angle (Fig. 2a), b is the blade height (Fig. 2c), e the blade width at the impeller inlet and outlet periphery (Fig. 2a) and t_{tc} the tip clearance thickness (Fig. 2c). The subscripts 1, 2 correspond to the inlet and the outlet of the impeller, respectively.

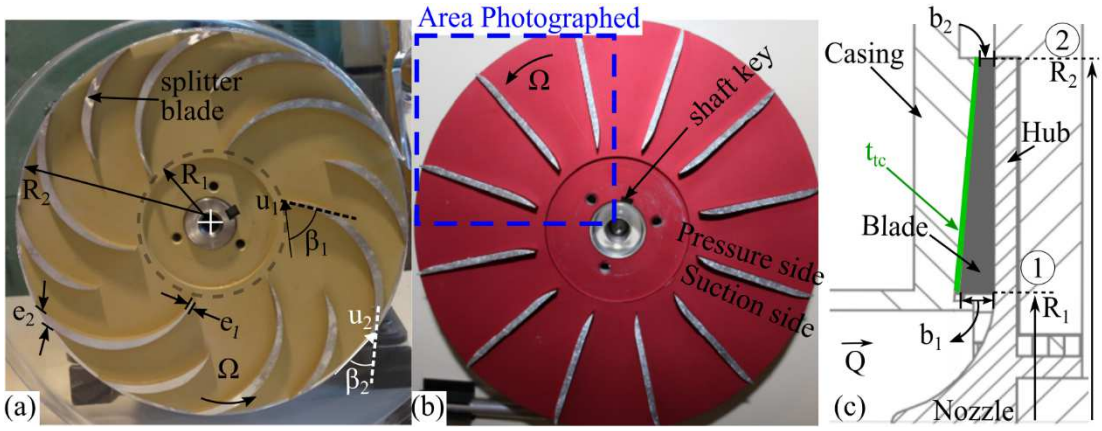

Fig. 2. a) Impeller No. 1, b) impeller No. 2, c) meridional view of the centrifugal pump.

The elbow pipe upstream of the pump inlet (Fig. 1(x)) introduces additional losses and causes a non-axisymmetric flow field at the pump inlet and in the rotating impeller, where cavitation onset appears at first at its left side. For this reason, the flow monitoring area is located at this side, as it is depicted in the blue area of Fig. 2b. The camera used is a DSLR type with 4752 x 3168 pixels, CMOS image sensor and max shutter speed 0.25 msec.

Two piezoelectric accelerometers, B01 (Fig. 1, ii) and A01 (Fig. 1, iii), are mounted on the casing of the pump, the first closer to the two-phase flow area and the second on the volute. The analog signal of both accelerometers passes through an analog low pass filter before its digitization in a MCC USB-1608G DAQ device. The sampling frequency, f_s, the cutoff frequency of the low pass filter, f_{cutoff}, the acquisition time, t_{acq} and the frequency range that each sensor is able to measure are given in Table 2.

Table 1. Design data of the impellers tested.

Imp. No.	Inlet/ Outlet	Blades No.	Splitter Blades.	R [mm]	β [deg]	b [mm]	e [mm]	t_{tc} [mm]
1	1	6	6	33	65	7.5	1.1	1
	2			82.5	25	3	10.1	
2	1	12	0	33	85	7.6	2.8	0.9
	2			82.5	90	3.1	5.9	

Table 2. Accelerometer and acquisition characteristics.

Sensor	f_s [kHz]	f_{cutoff} [kHz]	t_{acq} [sec]	[f_{min}-f_{max}] [Hz]
B01	20	10	30	0.2-15000
A01	20	5	30	0.2-10000

2.2 Testing procedure, performance equations and uncertainty estimation

The measurements aim at the derivation of the centrifugal pump cavitation characteristic curves, NPSH-H_{tot}, in their non-dimensional form, i.e. σ-Ψ, where σ is the Thoma cavitation factor and Ψ the head coefficient. These curves illustrate the variation of the total head of the pump, H_{tot} (Ψ) when the available net positive suction head of the establishment, NPSH (σ) decreases. Four curves at four different flowrates (Q) are derived for each impeller examined, following the open sump with throttle valve procedure that is provided from ISO 9906:2012 [49]. During this procedure, the level of static pressure in the testing configuration is progressively reduced by throttling the suction valve. The static pressure level of the establishment is described from NPSH available expression that is given in Eq. (1), where H_E is the pressure at the surface of the tank (Fig. 1, vii) in meters of water column, and $\Delta H_{z,e}$ the height difference between the pump suction (e) (Fig. 1) and the water level in the tank. The term $\zeta_e Q^2$ represents the hydraulic losses in the suction pipe, and H_{sat} the water saturation pressure expressed in mwc.

$$NPSH = H_{oe} - H_{sat} = H_E - \Delta H_{z,e} - \zeta_e Q^2 - H_{sat} \quad (1)$$

In practice, the implementation of the open sump with the throttle valve procedure increases the losses term ($\zeta_e Q^2$) of Eq. (1), and this in turn reduces the flowrate. For this reason, the discharge valve has to be properly regulated so as to restore the flowrate to its initial value and derive the σ-Ψ curves under constant flowrate conditions. This procedure introduces a limitation to the minimum attainable value of σ, when the discharge valve reaches its fully open position, because after that any further throttling of the suction valve reduces the flowrate and cannot be compensated. Thus the σ variation range becomes smaller at higher flowrates, where the testing starts with the discharge valve at more open position.

After 30 sec from the adjustment of the valves, the flow is stabilized and the flow conditions are considered as steady state. From that point, the flowrate, Q and the static pressure, p, at the suction (e) and the discharge (a) of the pump (Fig. 1) are recorded for a time period of 2 min, while the vibration signals are measured for 30 sec (Table 2). The measuring of the pressure and flowrate data allows for the calculation of NPSH and H_{tot} values, with the use of Eqs. 2 and 3, respectively:

$$NPSH = H_{oe} - H_{sat} = \frac{p_e}{\rho g} + \frac{8Q^2}{g\pi^2 d_e^{\,4}} - H_{sat} \tag{2}$$

$$H_{tot} = \frac{1}{\rho g}\left(p_a - p_e\right) + \frac{8Q^2}{\pi^2 g}\left(\frac{1}{d_a^{\,4}} - \frac{1}{d_e^{\,4}}\right) + z \tag{3}$$

where ρ is the water density, g the gravitational acceleration, d the pipe diameter and z the vertical distance between the discharge (α) and suction (e) static pressure measuring points. In the present study, the H_{sat} value is taken equal to 0.29 mcw that corresponds to 23ºC (the water temperature during the tests), z=0.305 m, and d_α=0.041 m and d_e=0.047 m. Finally, the Q, NPSH and H_{tot} values are non-dimensionalised using the flow coefficient Φ (Eq. (4)), the Thoma cavitation factor, σ (Eq. (5)) and the head coefficient Ψ (Eq. (6)), respectively:

$$\Phi = \frac{c_{2n}}{u_2} = \frac{1}{\omega R_2}\frac{Q}{\left(2\pi R_2 - z_s e_2\right) b_2} \tag{4}$$

$$\sigma = \frac{NPSH}{H_{tot}} \tag{5}$$

$$\Psi = \frac{2gH_{tot}}{u_2^{\,2}} \tag{6}$$

where c_n is the radial component of the absolute flow velocity, u is the tangential velocity of the impeller (Fig. 2a), and z_s the number of impeller blades.

During the time span of 2 min the macroscopic characteristics (position, shape and extent) of the cavitation area through the camera remain almost unchanged. As a result, the experimental photographs presented in this article are representative of the visually observed characteristics that the vapour phase exhibits during the 2 min of each measurement, even though the phenomenon microscopically exhibits transient features. It should be mentioned here that flow visualisation is used as a tool that confirms macroscopically the existence or absence of cavities, and its results are subjected to camera limitations. As a consequence, micro-cavities may exist microscopically even before the optical visual inception but the resolution of the camera could not depict them. All tests are performed three times in order to ensure the repeatability of measurements of the flow quantities, vibration and cavitation depiction.

The total relative uncertainty, $F(\varphi,t)$, of each measured (Q, p, T, n) flow and operating variable φ is calculated according Eq. (7) [50, 51]:

$$\begin{aligned} F\left(\varphi,t\right) &= \pm\sqrt{F\left(\varphi,s\right)^2 + F\left(\varphi,r\right)^2} = \pm\sqrt{F\left(\varphi,s\right)^2 + \left[\frac{\delta\left(\varphi,r\right)}{\varphi}\right]^2} = \ldots \\ \ldots &= \pm\sqrt{F\left(\varphi,s\right)^2 + \left(\frac{t\cdot S_\varphi}{\varphi}\right)^2} \end{aligned} \tag{7}$$

where $F(\varphi,s)$ is the systematic relative uncertainty, $F(\varphi,r)$ the random relative uncertainty, $\delta(\varphi,r)$ the absolute random uncertainty, S_φ the standard deviation and t the Student parameter [50]. $F(\varphi,r)$ and $\delta(\varphi,r)$ are associated with the Student's t distribution and with the uncertainty at the 95% confidence level, and they express the errors of repeated measurements obtained under unchanged machine's operating conditions. Finally, errors of the measured flow and operating variables are propagated in the calculations of NPSH, H_{tot}, Φ, σ and Ψ. The levels of total relative uncertainty of the above calculated quantities, are calculated based on the general formula (Eq. (8)) for error propagation. Accoding to this formula, the absolute error of a quantity φ derived from equation $\varphi=f(x,y,z)$, where x,y,z are variables with individual uncertainties, is given by:

$$\delta(\varphi,t)=\sqrt{\left[\frac{\partial\varphi}{\partial x}\delta(x,t)\right]^2+\left[\frac{\partial\varphi}{\partial y}\delta(y,t)\right]^2+\left[\frac{\partial\varphi}{\partial z}\delta(z,t)\right]^2} \tag{8}$$

In Table 3, the total relative uncertainty of all measured and calculated quantities is provided. The uncertainties of density ρ, gravity acceleration g, vertical distance z, impeller radius and suction and discharge pipe diameters are ignored. In general, the uncertainty values presented in Table 3 are low and ensure the reliability of the conclusions drawn from the cavitation tests on this particular test configuration.

Table 3. Total relative uncertainty of measured and calculated variables.

	Measured Variables					Calculated Variables				
φ	Q	p_e	p_α	T	n	Φ	Ψ	σ	H_{tot}	NPSH
±F(φ,t) [%]	0.6	0.3	0.3	1	0.1	0.6	0.6	0.8	0.6	0.6

3. Signal processing of the vibration data

In this section, the theoretical background of the SKT and the demodulation technique used in the dynamic measurements of the present study for the detection of cavitation, are provided. It is noted that the implementation of the signal processing tools is made in MATLAB proprietary programming language.

3.1 The Spectral Kurtosis tool

The aim behind the development of the SKT is the extraction of information related with a non-stationary process from a TS that presents Gaussian characteristics. The applicability of such a tool on the field of machine diagnostics lies in the fact that usually noise and vibration

signals measured for the detection of a fault contain information from multiple parts of the machine and resemble stationary random signals, such as white noise. At the same time, information related to a possible fault that exhibits highly impulsive non-Gaussian behaviour may be hidden in the original signal, and hence its extraction would be of critical importance to effectively detect this fault.

The use of higher-order statistics for the pattern recognition of non-stationary signals was firstly introduced by Dwyer [52-55] and dealt with underwater noise measurements. During the statistical analysis of noise signals, Dwyer observed that skewness and kurtosis values deviate from the values of Gaussian distribution. Dwyer also perceived that the representation of these statistical moments in the FS and, especially, the depiction of Spectral Kurtosis value could provide additional information for the source of non-stationarity. The complete mathematical formulation for the STFT estimation of Spectral Kurtosis, $\hat{K}_Y(f)$, is given by Antoni [47]:

$$\hat{K}_Y(f) \triangleq \frac{\left\langle \left| Y_w(kP, f) \right|^{4n} \right\rangle_k}{\left\{ \left\langle \left| Y_w(kP, f) \right|^{2n} \right\rangle_k \right\}^2} - 2 \tag{9}$$

where $Y_w(kP,f)^{xn}$ is the xn-th order empirical spectral moment of the STFT of a sampled process $Y(n)$, $w(n)$ is the analysis window, P is the temporal step and $\langle \ldots \rangle_k$ is the time averaged operator over index k, which denotes the number of temporal steps. Furthermore, in order to efficiently scan the FS and identify the filters characteristics, the Spectral Kurtosis is calculated for different frequency resolutions and all the results are plotted as function of frequency. This calculation is accomplished with the use of Fast Kurtogram (FK) that is introduced by Antoni [48], where the FS decomposition is made with the use of Eq. (10):

$$\delta f = 2^{(DL-1)}, \; DL = 0, ..., 7 \tag{10}$$

where δf is the frequency resolution and DL is the Decomposition Level. The final outcome of the calculations is a two-dimensional map of the value of Spectral Kurtosis (Fig. 3), calculated by Eq. (9), as function of frequency versus frequency resolution. The location and the maximum value of the Spectral Kurtosis for each DL changes as the original signal is divided at more and more segments. The Maximum Spectral Kurtosis (MSK) can be finally obtained at certain frequency range and DL (Fig. 3).

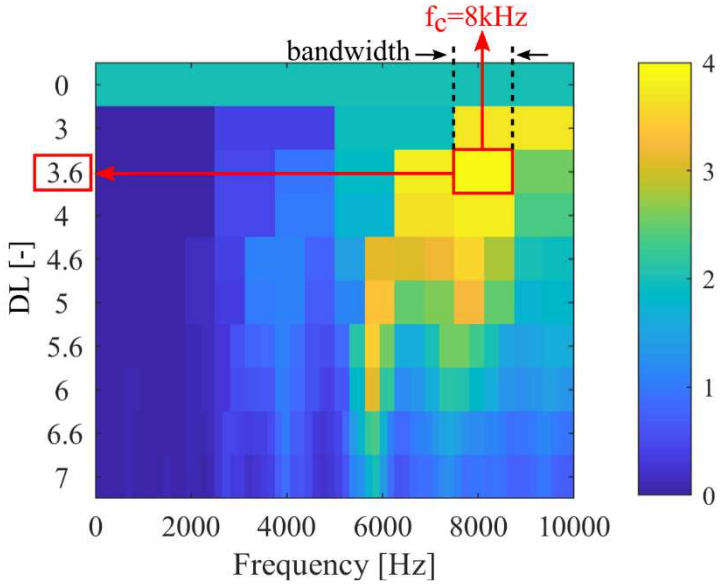

Fig. 3. Fast Kurtogram at the vibration signal of a centrifugal pump under cavitating conditions.

The FK designates the frequency and frequency resolution of the MSK value, which is information of crucial importance regarding the detection of non-stationarities. More specifically, those quantities correspond to the central frequency, f_c and the bandwidth of the band pass filter to be used for the isolation of the impulsive behaviour hidden in the sampled signal. In the case of Fig. 3, the MSK=4 corresponds to a band pass filter with f_c=8 kHz and 1.25 kHz bandwidth (DL=3.6).

3.2 Envelope analysis

The present study investigates the envelope characteristics in the frequency domain towards the detection of cavitation in hydraulic turbomachines. The signal processing approach adopted here is a typical demodulation or enveloping procedure, which is also used for the detection of rolling bearing faults that present impulsive characteristics, similarly to cavitation [56-59]. The demodulation procedure is carried out in the filtered signal, after the implementation of the SKT, in the following successive steps:

i. The Hilbert Transfomation is applied to the filtered signal, $x_f(t)$:

$$x_{Hf}(t) = \frac{1}{\pi} \int_{-\infty}^{+\infty} \frac{x_f(t)}{t-\tau} d\tau \tag{11}$$

ii. The analytic signal, $A_s(t)$ is formed with the use of Eq. (12), which consists of two parts; one real part that is the filtered signal, $x_f(t)$, and one imaginary part that is its Hilbert Transformation, calculated from step (i).

$$A_s(t) = x_f(t) + jx_{Hf}(t) \tag{12}$$

iii. The demodulated time signal is the amplitude of the analytic signal, i.e. the envelope of the filtered TS, calculated from Eq. (13):

$$e_d(t) = |A_s(t)| = \sqrt{x_f(t)^2 + x_{Hf}(t)^2} \tag{13}$$

iv. Finally, the ES can be calculated from Eq. (14):

$$e_d(f) = \int_{-\infty}^{+\infty} \sqrt{x_f(t)^2 + x_{Hf}(t)^2}\, e^{-j2\pi ft} dt \tag{14}$$

4. Cavitation σ-Ψ curves and flow visualisation results

The results of the σ-Ψ cavitation characteristic curves of the two impellers at four different flowrates are given in Fig. 4. It is noted that the blue and black color markers on these curves indicate the visual inception (σ_{VI}) of the first vapour bubble and the total head drop (σ_{FC}) conditions, respectively. The discussion of σ-Ψ curves is accompanied by the presentation of the flow visualisation results, which are given in Figs. 5 and 6, for the two impellers tested. These figures illustrate the development of cavitation visually obtained characteristics under σ_{VI} (left photograph), σ_{FC} (right photograph) and intermediate cavitating conditions (photograph in the middle). The photographs provided here correspond to one specific flowrate, but they can represent sufficiently the changes observed in the shape and the extent of the vapour area, during the testing of all loading conditions.

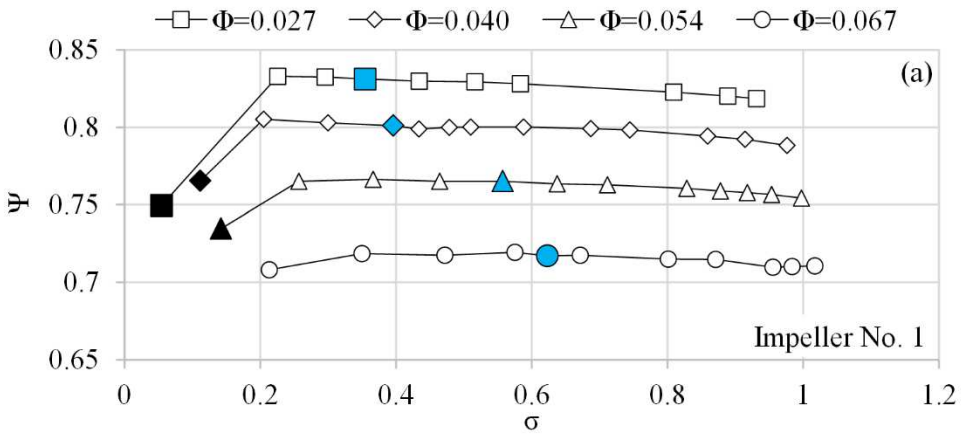

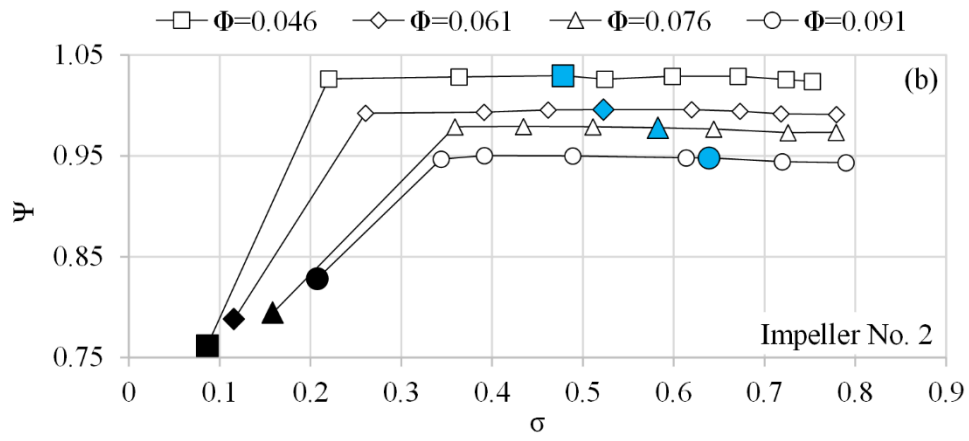

Fig. 4. Cavitation σ-Ψ characteristic curves for the two impellers at different Φ values.

For all cases tested the total head values (Ψ) remain unaffected by the reduction of σ value (Fig. 4), even after the formation of the first visually observed cavities at σ_{VI} (blue markers in Fig. 4 and Figs. 5a & 6a). Furthermore, for both impellers and all flowrates examined, the first small bubbles (blue circles drawn on Figs. 5 & 6) always appear at the suction side of the leading edge of the blades, where the minimum static pressure is developed that can drop below the water saturation pressure and inititate local evaporation [2, 4 & 60]. Although, the reduction of the cavitation factor value at intermediate cavitation conditions results in increased number of bubbles (Figs. 5b & 6b), the vapour area does not influences the power transfer to water, since Ψ remains constant, as when the pump operates under non-cavitating conditions (Fig. 4).

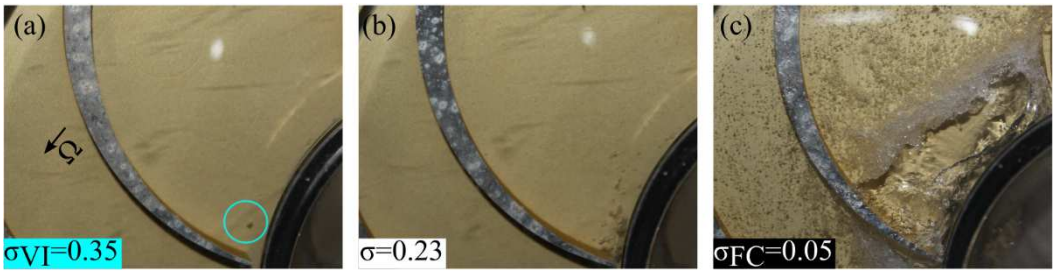

Fig. 5. Flow visualization results for impeller No. 1, at Φ=0.027.

However, reducing the suction available pressure at σ_{FC} (black colour markers in Fig. 4) results deterioration of the pump total head and confirms the general shape of the σ-Ψ curve that can be found in the literature [2, 4, 61]. The drop of Ψ, presented in Fig. 4, results from the creation of a large attached cavitation vapour bubble at the inlet of the impeller that reduces drastically the flow passage area between the adjasent blades, as well as spoils the hydrodynamic performance of the blade (Figs. 5 & 6). Only the head of the largest flowrate of Impeller No. 1 (Fig. 4a) does not show this behavior, due to the inability of the testing method to further reduce σ at higher flowrates, as discussed in section 2.2.

Fig. 6. Flow visualization results for impeller No. 2, at Φ=0.046.

Another observation from Fig. 4 is that for both impellers, an increase of the flowrate results in higher values of both σ_{FC} and σ_{VI}. This is because at higher flowrates in a specific impeller, the static pressures at the suction side of the pump reduce, hence favoring the vapour formation. Finally, vapour formations during σ_{FC} conditions at impeller No. 2 extend to a larger part of the flowpath (Fig. 6c) compared to impeller No. 1 (Fig. 5c) for two reasons, related to their geometrical characteristics; i) the larger number of blades (12, instead of 6) and ii) the higher inlet blade angle (85º instead of 65º). More specifically, the larger number of blades reduces the net flow passage area and accelerates the flow at the impeller inlet. On the other hand, the even higher inlet blade angle of impeller No. 2 than the relative flow incidence angle, increases the flow impact losses and local recirculation at the suction side of its blades, thus making the impeller more prone to cavitation.

5. Vibration measurement results

The results of the vibration data, which are obtained from the accelerometers on the pump casing (Fig. 1), are initially examined in the FS and in time, along with the behaviour of their statistical moments. The FS of the measured time signals are calculated with the use of Welch function [62]. In addition, the present study focuses on the application of the SKT and on the analysis of the filtered signals that result after the implementation of the band pass filters calculated from the FK. Finally, the filtered signals are further processed, so as to study the ES and to reveal the special characteristics introduced after the development of cavitation in the centrifugal pump. It should be noted that the cavitation tests include the investigation of four different flowrates for each impeller (Fig. 4), each of which consists of an average of ten operating points (OPs), while every point includes the vibration data of two accelerometers. Consequently, in order to reduce the number of the presented data, only part of the latter that adequately represents the vibration pattern of the impellers is selected for discussion. Similarly, regarding the raw vibration data and their statistical properties, the results of one impeller are presented, since they do not differentiate significantly when the blade geometry changes.

5.1 Detection based on time and frequency domain analysis

Figure 7 shows four raw vibration signals, obtained from sensor A01 under different suction conditions of impeller No.1; i) single-phase (Fig.7a), ii) cavitation inception, σ_{VI} (Fig. 7b), iii) intermediate cavitation (Fig. 7c), and iv) head break dwon, σ_{FC} (Fig. 7d). The TSs of Fig. 7 are focused in a short, indicative timespan (0.08 sec), in order to illustrate details such as the signal amplitude or possible strikes and impulses. Moreover, this time span is large enough to include the period of the main low frequency components created by the pump, such as the rotating frequency of the shaft (RF), the blade passing frequency (BPF) and the total blade passing frequency (TBPF). The latter is calculated only for impeller No.1 that contains a number of splitter blades. The values of RF, BPF and TBPF are given for each impeller in Table 4, along with their corresponding periodicities RP, BPP and TBPP.

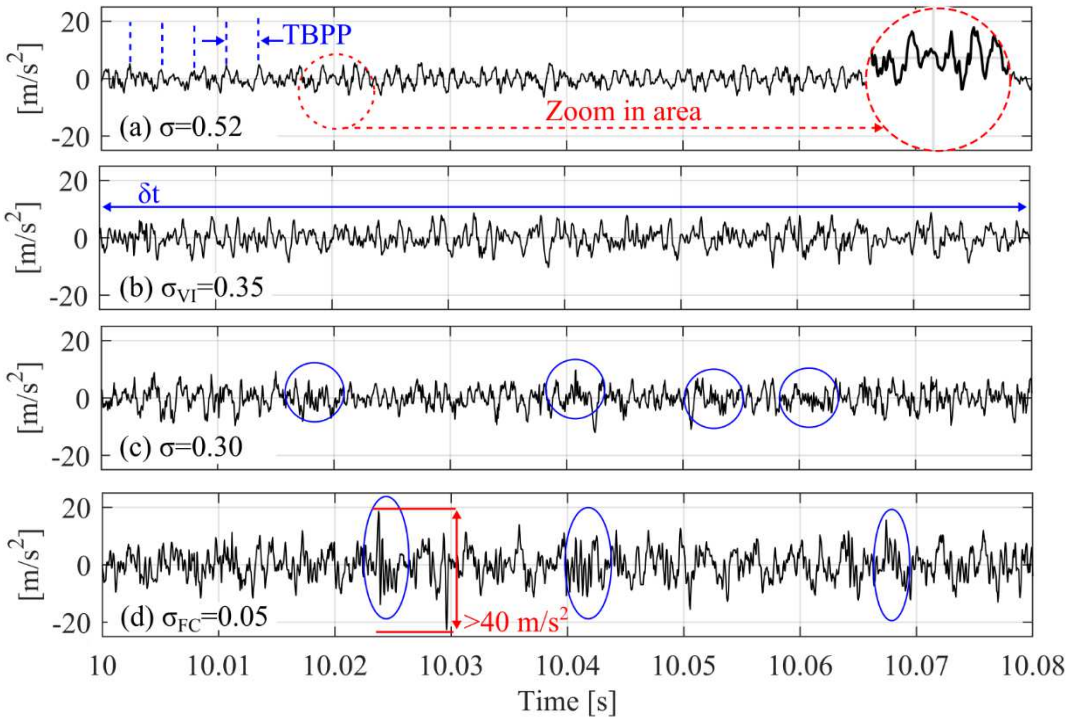

Fig. 7. Time series under various suction conditions for impeller No. 1, sensor A01, Φ=0.027.

Table 4 Frequencies and periodicities excited by the pump.

Impeller No.	RF [Hz]	RP [s]	BPF [Hz]	BPP [s]	TBPF [Hz]	TBPP [s]
1	30	0.033	180	0.0055	360	0.0027
2	30	0.033	360	0.0027	-	-

The vibration TS during non-cavitating conditions (Fig. 7a) are mainly formed by a synthesis of sinusoidal components that include the passing of the rotating blades, and its trend

for impeller No. 1 is depicted in this graph. Here, the signal pattern agrees with the expected vibration signature, which in hydraulic turbomachinery is usually modulated by RF, BPF and TBPF [63, 64] and should be a kind of sinusoidal, especially in the present pump that does not have embedded bearings (zoom in area of Fig. 7a).

The passing from non-cavitating to visual inception conditions, at σ_{VI} (Fig. 7b), does not change the signal pattern compared to Fig. 7a, except of a slight increase in the vibration amplitude, which, however, is difficult to be correlated with cavitation. Under such conditions, only few bubbles develop in the impeller and cover a very small part of the flowpath (Figs. 5a and 6a). Consequently, the overal vibration of the machine overrides that of pressure waves noise.

At intermediate cavitation conditions (Fig. 7c) and at head breakdown, σ_{FC} (Fig. 7d) some special characteristics appear in the vibration TS. When the pump operates at σ=0.30, the data include areas of small amplitude that make the signal to have a denser pattern (blue circles in Fig. 7c). Furthermore, at full cavitation conditions, where vapour bubbles cover a large part of the impeller flowpath (Figs. 5c & 6c), the vibration signature exhibits impulses of thin timespan with increased amplitude (blue ellipses in Fig. 7d), which are presumably associated with the implosion of vapour bubbles.

Although the analysis of the raw measured data of Fig. 7 provides some first indications that reveal the presence of cavitation, they cannot constitute a prompt cavitation detection criterion. The reason is that these indications are masked by the machine noise and cannot become easily observable at the early stages of cavitation development. As a result, further analysis of the signal properties must be carried out, in order to unmask and quantify new information related to cavitation mechanism, and its interaction with the flow conditions and the machine components.

An additional conclusion extracted from the TSs of Fig. 7, is that, regardless of the suction conditions, the combination of processes that compose the measured signals exhibit stationary characteristics in terms of their mean value, since the latter remain constant and does not change during the sampling time. In order to examine the development of possible non-stationarities in the rest statistical properties, the time-varying patterns of the standard deviation, skewness and kurtosis need to be calculated.

A practical way to calculate the time-varying behavior of the moments is through the splitting of the measured data in sampled groups that include the same number of raw data. In the present study, the signals are put in groups of 1000 raw data. For each group, the standard deviation, the skewness and the kurtosis are calculated, and in this way it is possible to illustrate their pattern in time that is now expressed in number of samples. After this processing, it is possible to examine whether their values remain constant (the moments describe a stationary process) or deviate in time (the moments describe a non-stationary process). The results that

correspond to impeller No.2, sensor B01, at Φ=0.061 are shown in Figs. 8a,b,c for the standard deviation, skewness and kurtosis, respectively.

As can be seen in Fig. 8a, the standard deviation value does not change as function of the number of samples (time) during constant suction conditions. Differences are only observable between the different σ values examined, where the standard deviation value increases with the development of cavitation in the pump. The latter depicts the effect of the impulses on the measured data, shown in Figs. 7c,d which increase the vibration amplitude range and, concequently, affect the standard deviation value. The skewness value in Fig. 8b does not deviate neither as function of time nor under different cavitating conditions.

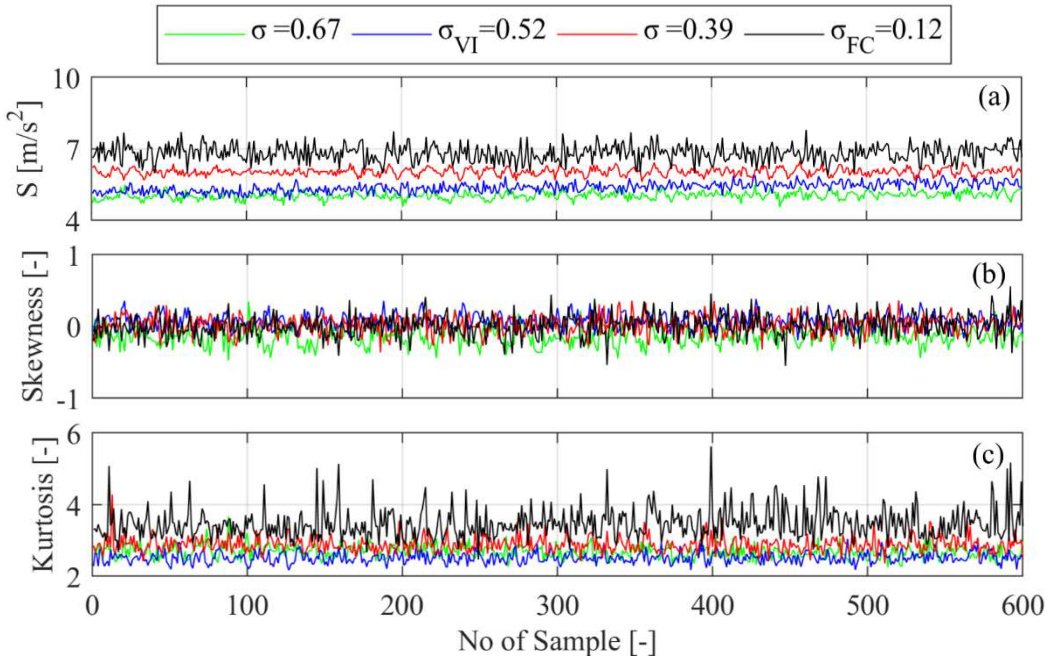

Fig. 8. a) Standard deviation, b) skewness and c) kurtosis values of the grouped data under various suction conditions for impeller No. 2, sensor B01, Φ=0.061.

On the contrary, the graph of Fig. 8c, reflects the highly transient behavior of kurtosis, when the impeller operates under intermediate (σ=0.39) and heavy cavitating (σ=0.12) conditions. More specifically, for non-cavitating (σ=0.67) and visual inception (σ_{VI}) conditions, the kurtosis values remain unchangeable and close to the normal distribution value (kurtosis=3). The closer the pump operates to the total head drop (σ_{FC}) point the stronger peaks are generated due to bubble implosion, making kurtosis to take values higher than 3. This conclusion is of crucial importance since it reveals the hidden non-stationarities resulted from two-phase flow development in the pump, which are not observable in the TSs of Fig. 7. The correlation of non-stationarities with the kurtosis value of the vibration data agrees with the results presented from Dwyer [52-55] and justifies the selection of kurtosis-related tools, such as the SKT presented in section 5.1, for the detection of cavitation.

The raw vibration data are also used to investigate the differences observed in the FS, due to cavitation development. The analysis makes use of semi-log plots (Fig. 9), where only the y-axis of the power distribution is shown in logarithmic scale. This approach is used by several researchers [11, 12, 21, 26 & 29], in order to highlight the differences observed in the low amplitude area of the vibration spectrum. The results for an indicative flowrate are given in Fig. 9 and include the spectra of various cavitating conditions for both impellers tested.

In these graphs it is clear that cavitation excites wide areas of the FS, regardless of the particular impeller and sensor mounting position. The excitations produced by the two-phase flow development (Fig. 9) are strongly related with the mechanism of cavitation, and more specifically, with the shock pressure waves created during the bubble implosion. It is important to underline that the excitations due to cavitation development do not refer to the increase of discrete frequency components, which appear in the high frequency range even before the cavitation development, at $\sigma>\sigma_{VI}$ (green line in Fig. 9). This is concluded after carefull examination of the spectrum and the observation of the existence of green peaks in the majority of the high frequency discrete components (Fig. 9).

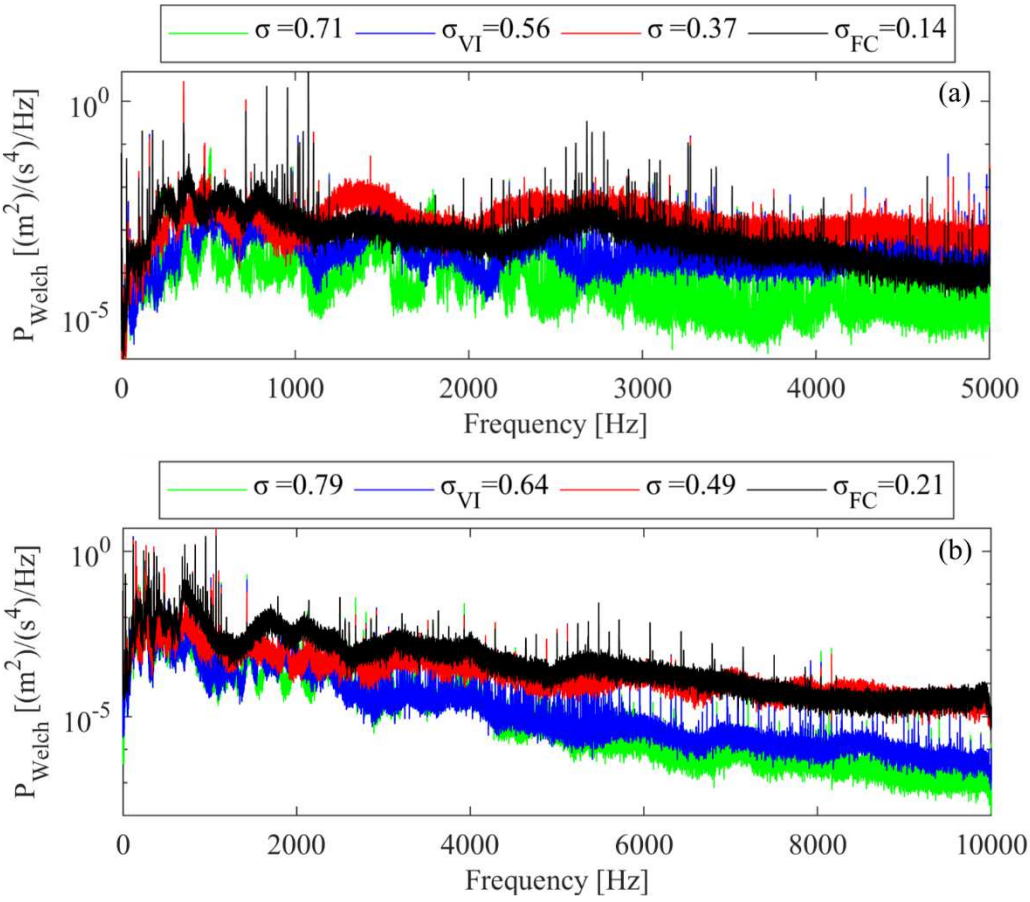

Fig. 9. Welch estimator of power spectral density under various suction conditions for a) impeller No. 1, sensor A01, Φ=0.054, and b) impeller No. 2, sensor B01, Φ=0.091.

In general, the changes in the characteristics of FS due to cavitation development are similar with those of the published literature for hydraulic turbomachines. Particularly the similarities with the results of Escaler [18-19] spectra that refer to Francis hydroturbine prototypes of 10 MW, reveal the analogies of the cavitation effect between the different types and size of hydaulic machines. However, despite the decent agreement with the published results, the intensity, the location and the range of excitations differentiate among the various testing configurations, machines, operating and suction conditions [11, 12, 18, 19, 21, 26 & 29].

The reason for such differences is that the FS excitations demonstrate mainly the symptom of the fault (cavitation development) rather than the actual mechanism, which in case of cavitation is the bubble implosion close to the rotating and stationary solid surfaces, and it is the same for every hydraulic turbomachine. On the other hand, the symptom (high frequency excitation) reveals the interaction of the fault mechanism with the pump structural characteristics, and consequently, it varies among various configurations. As a result, it is not possible to create a general detection cavitation criterion that could be broadly used in hydraulic turbomachinery applications.

Furthermore, as mentioned previously, there are faults related with rolling element bearing, which at some stage of their evolution excite wide range of high frequencies, up to 20 kHz, in a similar manner with cavitation. As a result, the FS analysis may result in incorrect conclusions regarding the determination of the type of damage that the hydraulic machinery suffers from. A practical way to distinguish the cavitation among the bearing faults is to operate the hydraulic turbomachine in lower (or higher) σ values, to study the changes on the FS. However, this procedure is not practical when dealing with industrial hydraulic turbomachines and consequently, the use of such tools can not provide a clear answer regarding cavitation development.

Therefore, additional effort is needed for a well-rounded characterization of cavitation that will include the identification of the phenomenon signature in time, and its correlation with a range of frequencies that will not change in different machines. In this direction, the results presented in this section, especially those that refer to kurtosis and to excitations of the frequency vibration spectrum, are further investigated, since they justify the use of SKT for cavitation detection and will be thoroughly discussed in the next section.

5.2 Detection based on the application of Spectral Kurtosis tool

The presentation of the results obtained by the application of SKT is divided in two parts. The first refers to the results of the FK and includes the calculations of the MSK, DL and band pass filter central frequency, f_c, values. The second part presents the results after the application of filtering and demodulation procedure, i.e. the TS and the ES of the filtered signals. In both parts the results are presented as function of the suction conditions at various flowrates. The

study focuses mainly on the initial and intermediate cavitating conditions ($\sigma_{VI} > \sigma > \sigma_{FC}$), where the effective and reliable detection of two-phase flow formation is a challenge.

5.2.1 Fast Kurtogram results

The results of the MSK, DL and f_c values as function of σ for a specific flowrate and sensor of each impeller are drawn in Fig. 10. The blue dashed line symbolizes the σ_{VI} OP, where two-phase flow area becomes visible in the impeller. According to these graphs, the MSK value does not exhibit the same trend for both impellers, after the onset of cavitation. More specifically, the MSK value of impeller No.1, remains relatively unchanged as the σ drops (Fig. 10a), whereas for impeller No.2 there is an abrupt increase of MSK at σ_{VI} (Fig. 10b), which, at smaller σ values exhibits a scattered behaviour, but keeps clearly higher values then under single-phase conditions ($\sigma > \sigma_{VI}$). This behaviour could be the result of the mechanism discussed in [7, 9, 11, 14] that deals with the noise absorption from the vapour phase at low σ values. This could affect in a similar manner the non-stationary characteristics of a vibration signal and, consequently, may reduce the MSK values.

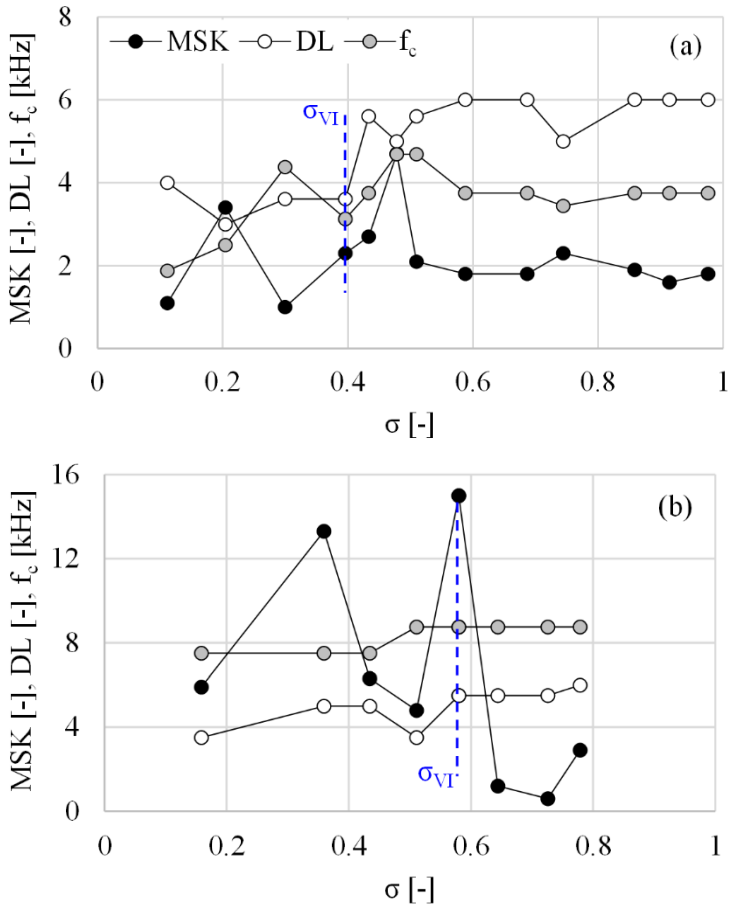

Fig. 10. MSK, DL and f_c values as a function of σ, for a) impeller No. 1, sensor A01, Φ=0.040 and b) impeller No. 2, sensor B01, Φ=0.076.

On the other hand, the DL and f_c curves presented also in Fig. 10, appear to decrease at lower σ values, no matter the flowrate, the sensor and the impeller under examination. Especially for the DL value, its drop during cavitating conditions seems to be in agreement with the conclusions made in Fig. 9, where the wide range excitations from cavitation are shown. These excitations are the results of vapour bubble implosion and drive the FK to identify the maximum kurtosis value in larger frequency ranges compared to those under non-cavitating conditions. Nevertheless, since other faults that exhibit impulsive behaviour, such as those related with bearings, are also expected to excite wide ranges of the spectrum [41, 42 & 65] justifies that such a drop of DL value occurs also during their development [48, 66 & 67]. Consequently, the decrease of DL value could be a strong sign that an impulsive fault develops in the machine (bearing or cavitation related), however, in order to identify the exact type of fault further analysis on the signal is required.

Finally, in order to provide an interpretation of the FK quantitative results presented in Fig. 10, the corresponding FK charts for OPs of a particular flowrate and sensor for each impeller are selected to be drawn in Fig. 11. The left FK chart corresponds to normal, and the right to cavitating flow conditions, for which the systematic shifting to lower DL and f_c values can be seen for both cases. The area with the MSK that is selected to be filtered after the FK calculations, is highlighted with a red rectangle in Fig. 11.

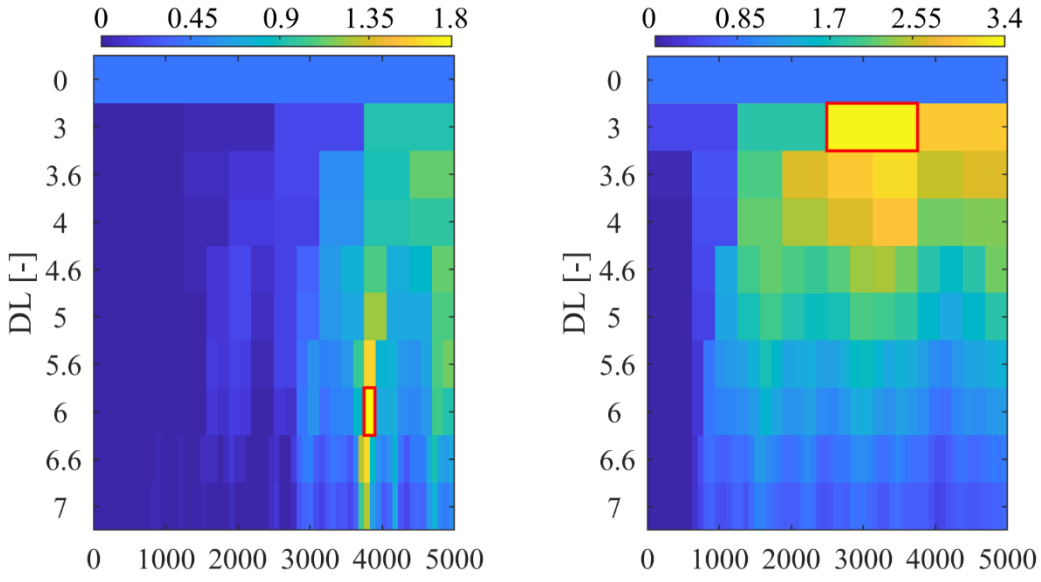

(a) **σ=0.98** (b) **σ=0.20**

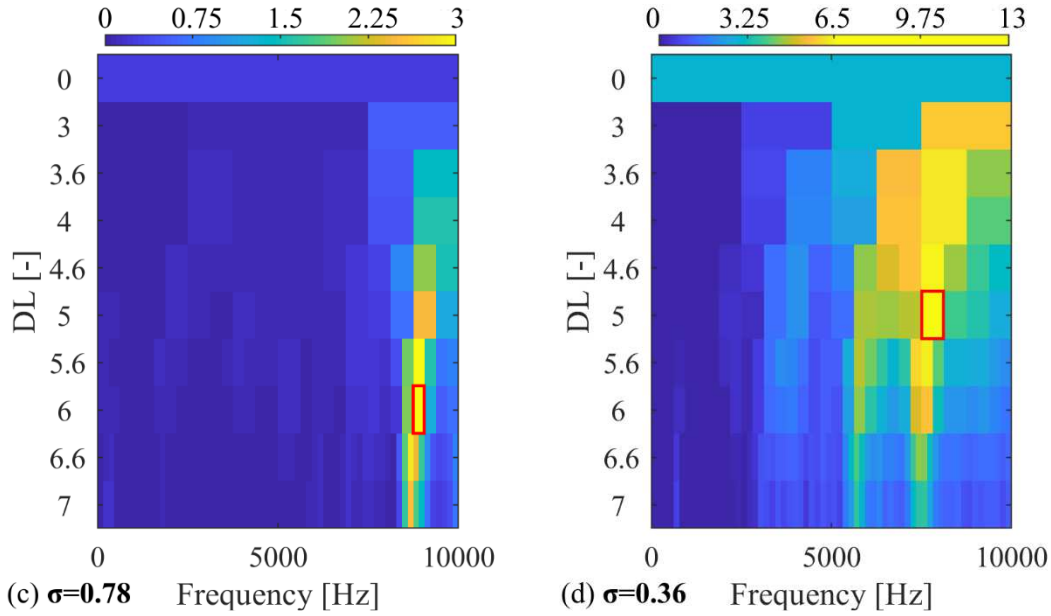

Fig. 11. Comparison of FK between a,c) normal and b,d) cavitating conditions for a,b) impeller No. 1, sensor A01, Φ=0.040 and c,d) impeller No. 2, sensor B01, Φ=0.076.

5.2.2 Filtered time signals

The filters obtained from the application of the FK tool are applied in the raw time signals. These are the same TS used by the FK tool for the calculation of the band pass filter characteristics, which are different for every OP (Fig. 10). The filtering procedure is evaluated based on the results of the TS and those of the ES. The reason for presenting the filtered results in the time domain is to examine their characteristics and investigate the possibility to distinguish cavitation from other possible faults.

The filtered time signals for the two impellers are presented in Figs. 12 and 13, during early and intermediate cavitating conditions, for $\sigma_{VI} > \sigma > \sigma_{FC}$. The results during non-cavitating conditions ($\sigma > \sigma_{VI}$) are also included for the lowest flowrate for comparison with the corresponding TS under cavitation. The timespan, δt, of the filtered series is kept equal to the plots of Fig. 7, so as to include all the characteristic frequencies excited by the centrifugal pump.

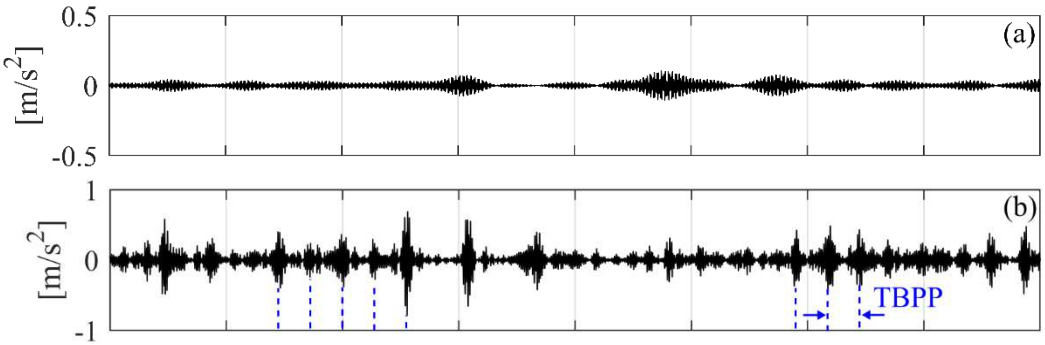

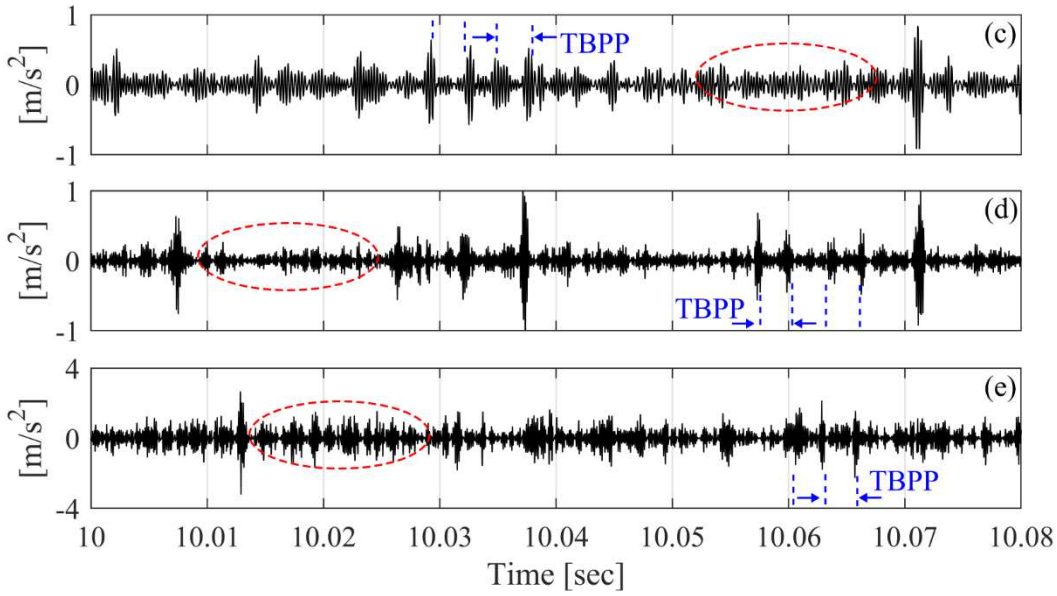

Fig. 12. Filtered time series for impeller No. 1 a) sensor A01, Φ=0.027, σ=0.43, b) sensor A01, Φ=0.027, σ=0.30, c) sensor B01, Φ=0.040, σ=0.30, d) sensor A01, Φ=0.054, σ=0.26, e) sensor B01, Φ=0.067, σ=0.58.

The filtered signals when the pump operates under single-phase conditions (Figs.12a and 13a) exhibit the minimum amplitude values compared to cavitating conditions (Figs. 12b-e & 13b-e), and do not present any distinctive characteristics. In practice, at such conditions the application of the filter made from the FK tool does not reveal a particular pattern in the filtered signal, since for $\sigma>\sigma_{VI}$ the machine is expected to operate at no fault conditions.

The first important observation regarding the filtered vibration time signals is that their pattern changes under cavitating conditions, for both impellers (Figs. 12b-e & 13b-e). The application of band pass filter calculated from the FK, reveals the existence of clear strikes in the filtered signal. Comparison of the filtered signal of Fig. 12b with its corresponding original time series presented in Fig. 7c, confirms the successful application of the filter, since the impulses are not observable in the raw measured vibration data. This observation is of paramount importance, since it reveals the impulsive pattern of cavitation mechanism that is masked in the original raw signal by various other noises of the pump. The decrease of the amplitude after filtering the signal is justified, considering the significant amount of noise and vibration sources removed from the band pass filter.

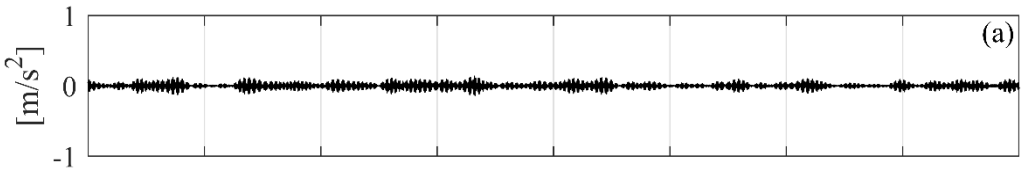

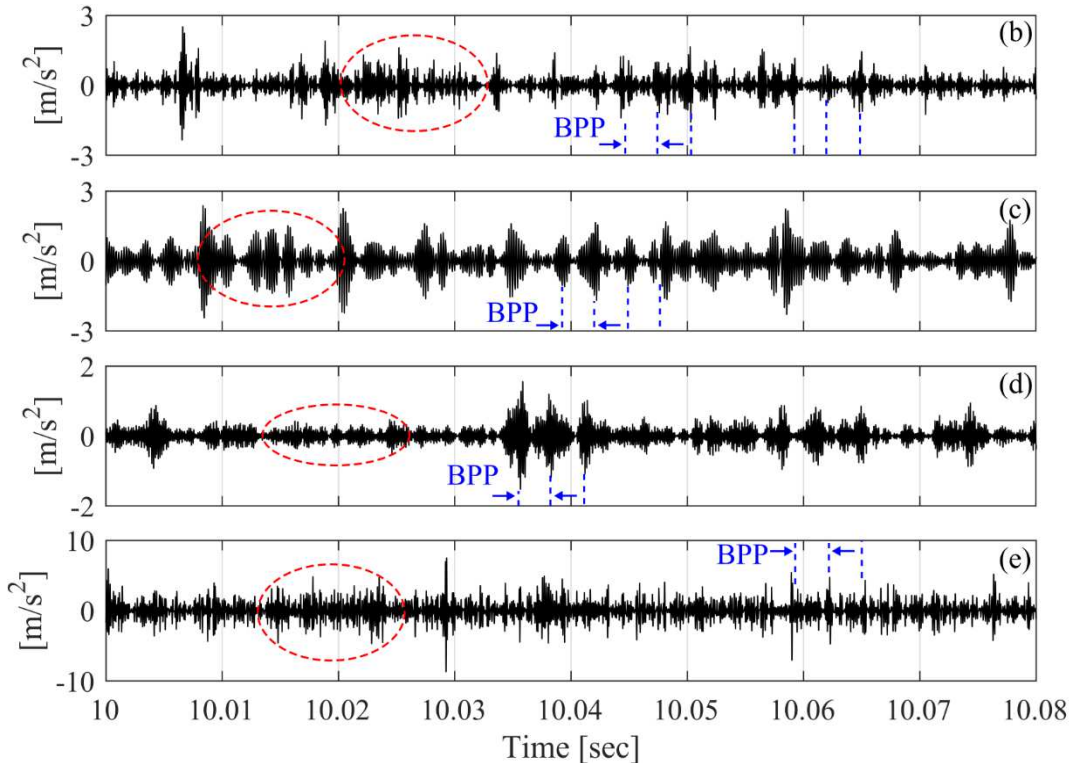

Fig. 13. Filtered time series for impeller No. 2, a) sensor B01, Φ=0.046, σ=0.52, b) sensor B01, Φ=0.046, σ=0.36, c) sensor A01, Φ=0.061, σ=0.39, d) sensor B01, Φ=0.076, σ=0.36, e) sensor A01, Φ=0.091, σ=0.39.

The amplitude of the filtered signals of Figs. 12b-e & 13b-e, does not present a clear dependence on the flowrate. The signals are formed by two main parts: one with low amplitude between the impulses, and one that includes the impulses' amplitudes that range from [0.4 – 3] and [1.5 – 9], for the impellers No. 1 and 2, respectively. The largest values for both impellers are obtained for the highest flowrate (Figs. 12e & 13e).

An additional observation regarding the TS presented in the filtered signals of Figs. 12 and 13, is that the area where the strikes are formed consists of random and periodic impulses. The latter follow mainly the blade passing frequency (BPF) of the impeller, and they are indicated with the blue dashed lines. On the other hand, impulses that are aperiodic are marked with red ellipses and indicate the random character of bubble implosion along with some distortion on the signal after the implementation of the filtering process. The enveloping process that is presented in the next section, attempts and succeeds to bring out the frequency that modulates the bubble implosion.

The correlation of the aforementioned impulses with cavitation phenomenon is further validated by studying the TS at σ_{FC} (Fig. 14). At such operating conditions the cavitation area is expanded and covers large part of the flow path between the blades, as it is depicted in Figs. 5c and 6c, and dominates the vibration signal. In the plots of Fig. 14 the periodic with the blade passing frequency and, simultaneously, the impulsive behavior of TS can be clearly observed.

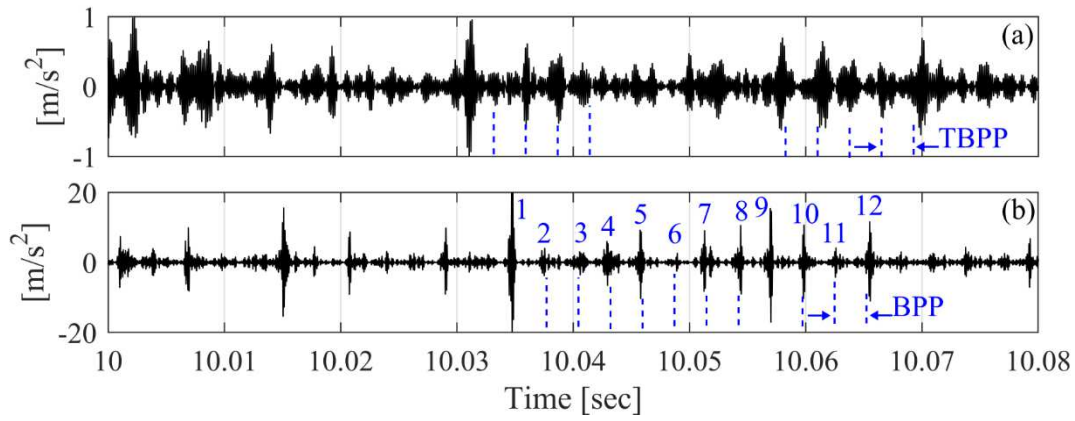

Fig. 14. Filtered time series for a) impeller No. 1, sensor B01, Φ=0.027, σ=0.05, b) impeller No. 2, sensor A01, Φ=0.046, σ=0.09.

In addition, the strikes of Fig. 14 are more clear and frequent than those presented in Figs. 12 and 13. Especially for the impeller No. 2 (Fig. 14b), the effect of passing of each of the 12 blades is highlighted. The impulsive shape of the strikes of these plots resembles the shape of the filtered vibration signal, presented in [68 & 69], which corresponds to rolling element bearings fault. Therefore, in order to be able to discriminate the bearing fault and the cavitation impulsive behaviour, the use of the periodicity of the impulses is proposed, since cavitation follows the blade passing frequency. However, as it is shown in the impulses of Figs. 12 and 13, during the initial stages of cavitation development the BPF periodicity is not always so clear, and hence, the ES is also used to extract the aforementioned information from the filtered signal.

5.2.3 Envelope spectra of the filtered signals

The ES of the filtered vibration signals is calculated from Eq. (14), and it is presented in Figs. 15 and 16, for three different σ values and four flowrates. The green colour corresponds to non-cavitating conditions ($\sigma>\sigma_{VI}$), while the red and black to initial (σ_{VI}) and intermediate cavitating conditions ($\sigma_{VI}>\sigma>\sigma_{FC}$), respectively. These plots include the spectra of both accelerometers, A01 and B01, used in the cavitation tests.

The results of the ES demonstrate the applicability of the digital band pass filter, achieved after the calculation of MSK value in the FK and the decomposition of the filtered signal. More specifically, no matter the impeller, the sensor, and the flowrate examined (Figs. 15 and 16), the ES exhibits significant differences when comparing non-cavitating with cavitating conditions. These differences are systematically related with the appearance of strong blade passing frequency components (BPF for impeller No.2, Fig. 16 & TBPF for impeller No. 1, Fig. 15), when the pump operates at intermediate cavitating conditions ($\sigma_{VI} > \sigma > \sigma_{FC}$).

The above behavior is critical, because not only differentiates the envelope's characteristics after cavitation development, but also associates these characteristics with the blade passing frequency of the impeller, and further confirms the results of the filtered signal analysed in the previous section 5.2.2. Furthermore, the clear appearance of these differences in the ES makes them utilizable for cavitation detection by an automated system.

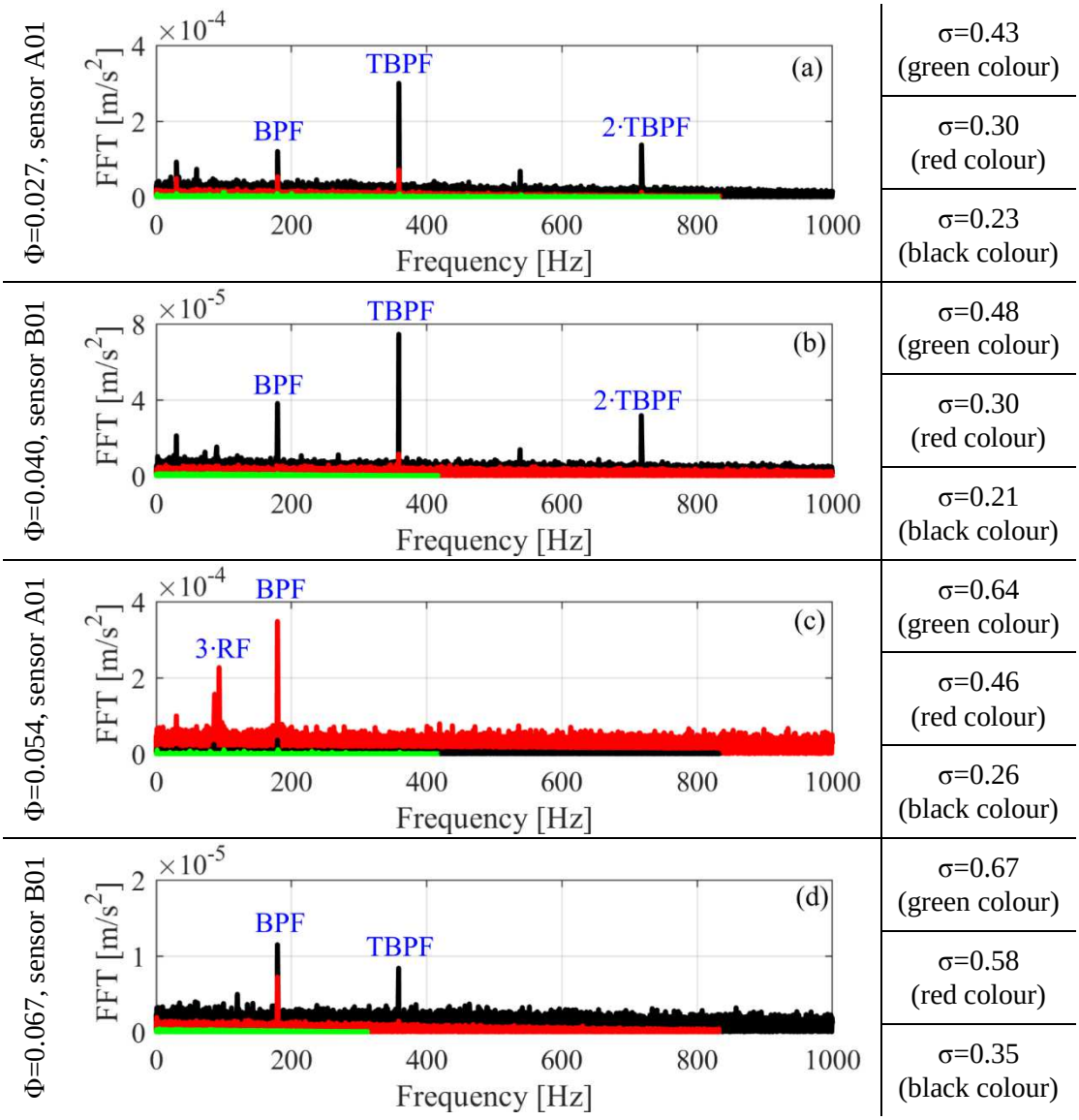

Fig. 15. Frequency domain of the envelope of the vibration signal of impeller No. 1.

The BPF modulation resembles the envelope characteristics, presented also in [19, 39] during the testing of reaction hydroturbines. More specifically, in these studies the vortex rope cavitation in the draft tube is associated with the 0.27·RF discrete frequency component, while the cavitation in the runner have been associated with the blade and guide vane passing frequencies. However, in these cases the characteristics of the filters are taken from the examination of the measured signal spectrum, an approach that has been proved to be complicated in the present study (Fig. 9), but also from the FS of similar studies [11, 12 & 16].

The successful implementation of Spectral Kurtosis method with the FK tool overcomes the aforementioned difficulties and achieves to define the filter's characteristics efficiently, in cases where it would be impossible to define them otherwise.

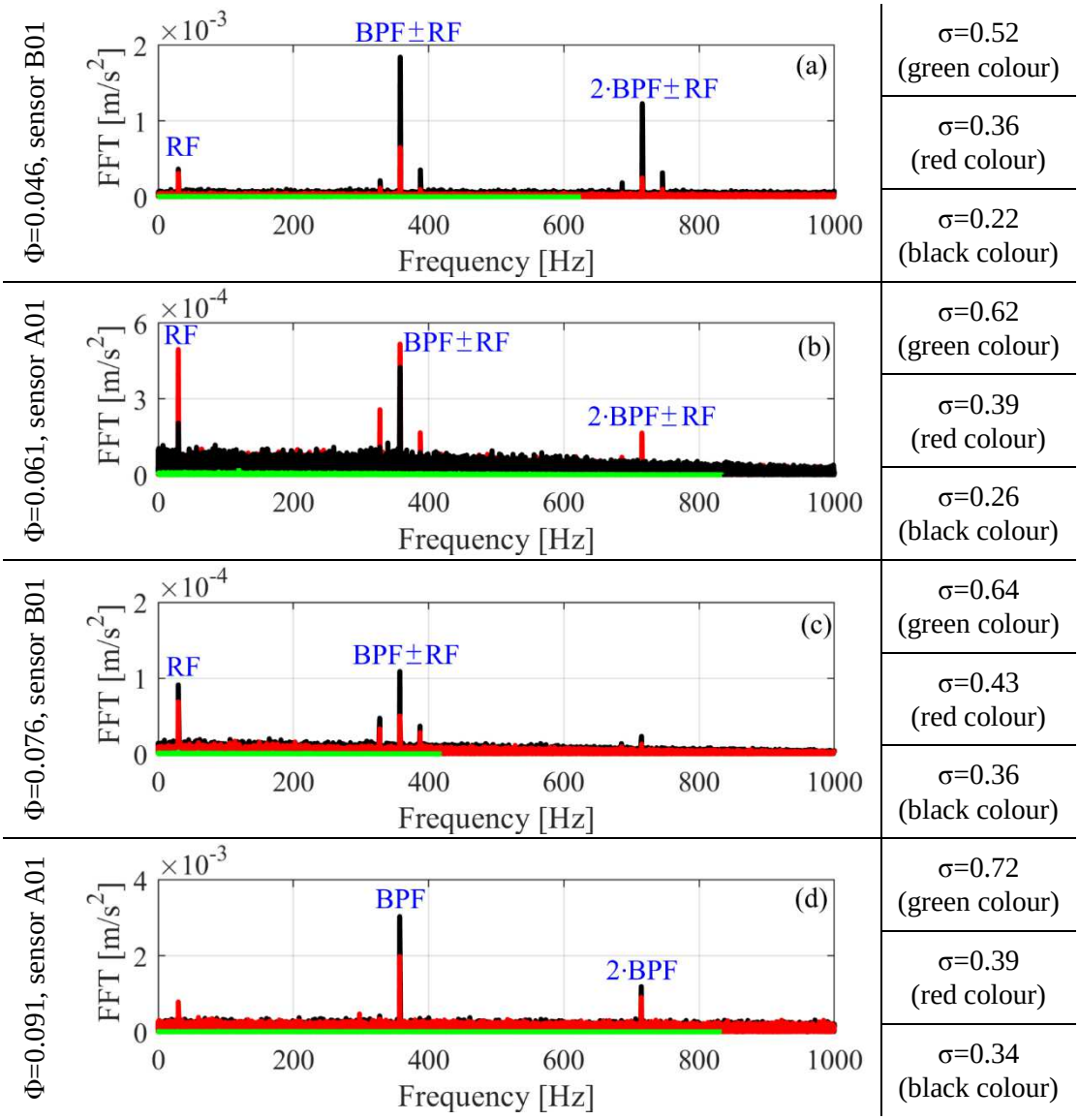

Fig. 16. Frequency domain of the envelope of the vibration signal of impeller No. 2.

The comparison of the amplitudes of the same sensor between the different impellers, depicts a rise of vibration intensity, from the lowest values of impeller No. 1 [$10^{-5} – 4 \cdot 10^{-4}$, Fig. 15], to the maximum values of impeller No.2 [$10^{-4} – 4 \cdot 10^{-3}$, Fig. 16]. Therefore, this is the result of the geometric differences of the two impelleres. More specifically, the amplitutes minimise for impeller No. 1 (Fig. 15) due to: i) the use of splitter blades that increases the cross section area of the flow path between the blades and, consequently, reduces the flow velocity at the impeller inlet, and ii) the smaller blade inlet angle that reduces the inlet flow shock losses. A second harmonic that appears in the ES of impeller No. 2 (Fig. 16), could be associated with

the stronger characteristics of cavitation in this pump. In addition, in the majority of the ES of both impellers, a weaker RF component can be observed (Figs. 15a-c & 16) that highlights the relation of the phenomenon with the rotational periodicity.

To sum up, the appearance of the passing frequency of the impeller blades is clear after the inception of cavitation. This behaviour is observed in the filtered time series of section 5.2.2 and it is further confirmed after their demodulation. Therefore, the identification of the impulses in the filtered signal, which are produced due to implosion of the vapour bubbles, and then modulated by the blade passing frequency, can be used to detect cavitation from the initial and intermediate stages of its development, but also they highlight the physical mechanism of the fault, which is the implosion of the vapour bubbles. More specifically, the bubbles are formed at the suction side of the impeller's blade (Figs. 5 & 6) and their implosion is followed by the creation of shock pressure waves. The waves hit the neighbouring solid surfaces, which for the impeller are the rotating blades. The latter rotate and due to the machine's non-uniformities, create blade passing frequency noise that modulates the shock pressure waves. Consequently the raw vibration signal measured on the solid boundaries of the pump includes the above information, along with additional noise from the pump-motor system. The application of the procedure described in this section achieves the unmasking of the noise sources and reveals the interaction of cavitation with the rotation of the blades.

The combination of the systematic characteristics in the filtered signal and the spectrum of the envelope with the physical meaning of the fault mechanism create a unique detection criterion. To our knowledge, there have not been reported any fault mechanisms related with centrifugal pumps and reaction hydroturbines that excite an impulsive, BPP periodic behaviour. In the published literature, there are mechanisms (rotor-stator interaction) related with a BPP periodic behaviour, which take sinusoidal form but they could not be impulsive. On the other hand, in the case of faulty bearings, the pattern of fault mechanism is strongly impulsive, however, its periodicity does not follow BPP but the kinematic bearing frequencies [66 & 68].

6. Conclusions

In this study, the Spectral Kurtosis methodology is applied for the detection of cavitation in centrifugal pump impellers. Two semi-open radial impellers are tested and their cavitation curves for various flowrates are derived. At each operating point, the vibration signal from two sensors at different positions is recorded and processed in time, in frequency domain and with the use of SKT. The research focuses on the fault detection at the initial and intermediate stages of cavitation development, before the collapse of the pump's total head.

The examination of the raw signals under heavy cavitating conditions reveals the presence of impulses that increase the vibration amplitude range. This is a typical symptom of fault in rotating machinery, while in the controlled tests of this study, the impulses appeare only after

passing into fully developed cavitation operating condition.s In addition, the analysis of the statistical properties of the vibration signals highlights the effect of cavitation development on the transient behaviour of the kurtosis of the population. The next step of the signal processing includes the study of the frequency spectrum, where significant differences between the normal and cavitating conditions appeare. However, the deviation of the excitation range and location in the spectrum at different suction conditions, as well as the strong similarities with the vibration spectrum of fault bearings, question significantly the use of such processing method.

On the other hand, the results of the SKT reveal the capability of the method to correlate vapour formation in the impeller with the appearance of BPF at the frequency spectrum of the envelope, and also to identify the impulsive signature of cavitation in the filtered time domain. The filtered signal in time is formed by random and periodic impulses, which are masked from various noise sources in the original signal. Nevertheless, the successful implementation of SK method allows their extraction. The aforementioned behavior of ES and TS is accompanied by the drop of signal Decomposition Level, observed in all examined cases. This drop confirms, from the filter construction perspective, the excitation of wider frequency bands after the development of cavitation.

The appearance of the aforementioned characteristics in the TS and the ES are systematic for both impellers tested, no matter the flowrate conditions, and demonstrates the modulation of the filtered signal from the periodicity of the rotating blades. The combination of the identification of the strikes that appear in the filtered signal, which are periodic with the BPF, along with the appearance of BPF discrete frequency in the envelope's spectrum, constitutes a general and robust cavitation detection criterion that can be used in centrifugal pumps. This behaviour of the filtered vibration signal is unique, since in the motor-coupling-pump system only the bearings could excite impulses, however they are modulated by different frequencies. Moreover, the fault mechanism (vapour bubble implosion) and the motor-pump system is analogous to that of the hydroturbine-generator, and this enables the application of the same criterion towards the detection of cavitation in hydroturbines.

Further tests and measurements in centrifugal pumps and hydroturbines of various specific speed, size and suction characteristics are required in order to evaluate the effectiveness and the generality of this new methodology for early cavitation detection.

Acknowledgements

This research has been co-financed by the European Union and Greek national funds through the Operational Program Competitiveness, Entrepreneurship and Innovation, under the call RESEARCH–CREATE–INNOVATE (project code: T1EDK-01334)

References

[1] S. C. Li, Cavitation of hydraulic machinery (Vol. 1), World Scientific, 2000.

[2] C. E. Brennen, Hydrodynamics of pumps, Cambridge University Press, 2011.

[3] C. E. Brennen, Fundamentals of multiphase flow, Cambridge University Press, 2005.

[4] J. F. Gülich, Centrifugal pumps (Vol. 2), Springer, Berlin, 2008.

[5] B. Schiavello, F.C. Visser, Pump cavitation - Various NPSHR criteria, NPSHA margins, and impeller life expectancy, 25th Int. Pump Users Symp. (2009) 113–143. https://doi.org/10.21423/R1XM30.

[6] Y.L. Zhang, S.Q. Yuan, J.F. Zhang, Y.N. Feng, J.X. Lu, Numerical investigation of the effects of splitter blades on the cavitation performance of a centrifugal pump, IOP Conf. Ser. Earth Environ. Sci. 22 (2014). https://doi.org/10.1088/1755-1315/22/5/052003.

[7] G. Mousmoulis, N. Karlsen-Davies, G. Aggidis, J. Anagnostopoulos, D. Papantonis, Experimental analysis of the onset and development of cavitation in a centrifugal pump, In Journal of Physics: Conference Series. 813 (2017). https://doi.org/10.1088/1742-6596/813/1/012044.

[8] D. Liang, Z. Yuqi, D. Cui, W. Yong, Research on cavitation acoustic characteristics of centrifugal pump based on fluid-acoustic field coupling method, Adv. Mech. Eng. 10 (2018) 1–13. https://doi.org/10.1177/1687814018773665.

[9] G. Mousmoulis, N. Karlsen-Davies, G. Aggidis, I. Anagnostopoulos, D. Papantonis, Experimental analysis of cavitation in a centrifugal pump using acoustic emission, vibration measurements and flow visualization, Eur. J. Mech. B/Fluids. 75 (2019) 300–311. https://doi.org/10.1016/j.euromechflu.2018.10.015.

[10] C. E. Brennen, Cavitation and bubble dynamics, Cambridge University Press, 2014.

[11] J. Cernetic, J. Prezelj, M. Chudina, Use of noise and vibration signal for detection and monitoring of cavitation in kinetic pumps, The Journal of the Acoustical Society of America. (2008).

[12] M. Chudina, J. Prezelj, Detection of cavitation in operation of kinetic pumps. Use of discrete frequency tone in audible spectra, Appl. Acoust. (2009). https://doi.org/10.1016/j.apacoust.2008.07.005.

[13] S.N. Ganeriwala, V. Kanakasabai, Using vibration signatures analysis to detect cavitation in centrifugal pumps, Rotating Machinery, Structural Health Monitoring, Shock and Vibration, Volume 5, Shock. 5 (2011) 307–324. https://doi.org/10.1007/978-1-4419-9428-8.

[14] N. Zhang, M. Yang, B. Gao, Z. Li, Vibration characteristics induced by cavitation in a centrifugal pump with slope volute, Shock and Vibration (2015). https://doi.org/10.1155/2015/294980

[15] A.M. Abdulaziz, A. Kotb, Detection of pump cavitation by vibration signature, Aust. J. Mech. Eng. 15 (2017) 103–110. https://doi.org/10.1080/14484846.2015.1093261.

[16] J. Lu, X. Liu, Y. Zeng, B. Zhu, B. Hu, S. Yuan, H. Hua, Detection of the flow state for a centrifugal pump based on vibration, Energies. 12 (2019). https://doi.org/10.3390/en12163066.

[17] A.R. Al-Obaidi, Investigation of effect of pump rotational speed on performance and detection of cavitation within a centrifugal pump using vibration analysis, Heliyon. 5 (2019) e01910. https://doi.org/10.1016/j.heliyon.2019.e01910.

[18] X. Escaler, E. Egusquiza, M. Farhat, F. Avellan, Vibration cavitation detection using onboard measurements, Fifth International Symposium on Cavitation. (2003).

[19] X. Escaler, E. Egusquiza, M. Farhat, F. Avellan, Cavitation erosion prediction in hydro turbines from onboard vibrations, 22nd IAHR Symposium on Hydraulic Machinery and Systems (2004).

[20] K. Wu, Y. Xing, N. Chu, P. Wu, L. Cao, D. Wu, A carrier wave extraction method for cavitation characterization based on time synchronous average and time-frequency analysis, J. Sound Vib. 489 (2020) 115682. https://doi.org/10.1016/j.jsv.2020.115682.

[21] M. Chudina, Noise as an indicator of cavitation in a centrifugal pump, Acoustical physics (2003) 463-474.

[22] D.P. Sloteman, Cavitation in high energy pumps-Detection and assessment of damage potential, In Proceedings of the 23rd International Pump Users Symposium (2007).
[23] S. Gopalakrishnan, Modern cavitation criteria for centrifugal pumps, In Proceedings of the 2nd International Pump Symposium. (1985). https://doi.org/10.21423/R1NT3K.
[24] P.J. McNulty, I.S. Pearsall, Cavitation inception in pumps, Journal of fluids engineering 104(1982) 99-104. https://doi.org/10.1115/1.3240865.
[25] L. Alfayez, D. Mba, Detection of incipient cavitation and the best efficiency point of a 2.2 MW centrifugal pump using Acoustic Emission, Journal of Acoustic Emission (2004).
[26] M. Chudina, J. Prezelj, Detection of cavitation in situ operation of kinetic pumps: Effect of cavitation on the characteristic discrete frequency component, Appl. Acoust. (2009). https://doi.org/10.1016/j.apacoust.2009.04.001.
[27] J. Cernetič, M. Chudina, Cavitation noise phenomena in centrifugal pumps, In 5th Congress of Alps-Adria Acoustics Association (2012).
[28] L. Dong, Y. Zhao, C. Dai, Detection of inception cavitation in centrifugal pump by fluid-borne noise diagnostic, Shock Vib. 2019 (2019). https://doi.org/10.1155/2019/9641478.
[29] G. D. Neill, R. L. Reuben, P. M. Sandford, E. R. Brown, J. A. Steel, Detection of incipient cavitation in pumps using acoustic emission, Proceedings of the Institution of Mechanical Engineers, Part E: Journal of process mechanical engineering. 211(1997) 267-277. https://doi.org/10.1243/0954408971529737.
[30] S.A. Al-Hashmi, Spectrum analysis of acoustic signals for cavitation detection, ISIEA 2012 - 2012 IEEE Symp. Ind. Electron. Appl. (2012) 321–325. https://doi.org/10.1109/ISIEA.2012.6496652.
[31] T. Cencîc, M. Hoĉevar, B. Ŝirok, Study of erosive cavitation detection in pump mode of pump-storage hydropower plant prototype, J. Fluids Eng. Trans. ASME. 136 (2014). https://doi.org/10.1115/1.4026476.
[32] H. Schmidt, O. Kirschner, S. Riedelbauch, J. Necker, E. Kopf, M. Rieg, G. Arantes, M. Wessiak, J. Mayrhuber, Influence of the vibro-acoustic sensor position on cavitation detection in a Kaplan turbine, IOP Conf. Ser. Earth Environ. Sci. 22 (2014). https://doi.org/10.1088/1755-1315/22/5/052006.
[33] P. Bourdon, R. Simoneau, J.M. Dorey, Accelerometer and pit counting detection of cavitation erosion on a laboratory jet and a large Francis turbine, XVII IAHR Symposium (1994) 599–615.
[34] X. Escaler, J. V Ekanger, H.H. Francke, M. Kjeldsen, T.K. Nielsen, Detection of Draft Tube Surge and Erosive Blade Cavitation in a Full-Scale Francis Turbine, Journal of Fluids Engineering (2015). https://doi.org/10.1115/1.4027541.
[35] Z. Hongbin, L. Hui, Diagnosis of Preliminary Cavitation In Pumps By Wavelet Analysis, Energy Resource and Power Engineering. (2010) 394-398.
[36] A. Hajnayeb, R. Azizi, A. Ghanbarzadeh, M. Changizian, Vibration-based cavitation detection in centrifugal pumps, Diagnostyka. 18 (2017) 77–83.
[37] R. Azizi, A. Hajnayeb, A. Ghanbarzadeh, M. Changizian, Cavitation Severity Detection in Centrifugal Pumps, In International Congress on Technical Diagnostic. (2016) 47-55. https://doi.org/10.1007/978-3-319-62042-8_4.
[38] H. Sun, S. Yuan, Y. Luo, Cyclic Spectral Analysis of Vibration Signals for Centrifugal Pump Fault Characterization, IEEE Sens. J. 18 (2018) 2925–2933. https://doi.org/10.1109/JSEN.2018.2804908.
[39] X. Escaler, E. Egusquiza, T. Mebarki, F. Avellan, M. Farhat, Field Assessment of Cavitation Detection Methods in Hydropower Plants, Proc. Hydraul. Mach. Syst. 21 St IAHR Symp. Sept. 9 (2002) 12.
[40] P.D. McFadden, J.D. Smith, Vibration monitoring of rolling element bearings by the high-frequency resonance technique - a review, Tribol. Int. 17 (1984) 3–10. https://doi.org/10.1016/0301-679X(84)90076-8.
[41] H. Prashad, M. Ghosh, S. Biswas, Diagnostic Monitoring of Rolling-Element Bearings by High-Frequency Resonance Technique, ASLE transactions (2008). https://doi.org/10.1080/05698198508981641.

[42] L. Saidi, J. Ben Ali, M. Benbouzid, E. Bechhoefer, The use of spectral kurtosis as a trend parameter for localized bearing fault diagnosis in induction machines, ISA Trans. 63 (2016) 436–447. https://doi.org/10.1016/j.isatra.2016.02.019.
[43] C. Yiakopoulos, K. Gryllias, I. Antoniadis, Spectral effects of the slip motion in defective rolling element bearings. Advances in Vibration Engineering (2005) 199-211.
[44] L. Xiao, X. Zhang, S. Lu, T. Xia, L. Xi, A novel weak-fault detection technique for rolling element bearing based on vibrational resonance, J. Sound Vib. 438 (2019) 490–505. https://doi.org/10.1016/j.jsv.2018.09.039.
[45] S. Lu, P. Zheng, Y. Liu, Z. Cao, H. Yang, Q. Wang, Sound-aided vibration weak signal enhancement for bearing fault detection by using adaptive stochastic resonance, J. Sound Vib. 449 (2019) 18–29. https://doi.org/10.1016/j.jsv.2019.02.028.
[46] L. Xiao, J. Tang, X. Zhang, T. Xia, Weak fault detection in rotating machineries by using vibrational resonance and coupled varying-stable nonlinear systems, J. Sound Vib. 478 (2020) 115355. https://doi.org/10.1016/j.jsv.2020.115355.
[47] J. Antoni, The spectral kurtosis: A useful tool for characterising non-stationary signals, Mech. Syst. Signal Process. 20 (2006) 282–307. https://doi.org/10.1016/j.ymssp.2004.09.001.
[48] J. Antoni, Fast computation of the kurtogram for the detection of transient faults, Mech. Syst. Signal Process. 21 (2007) 108–124. https://doi.org/10.1016/j.ymssp.2005.12.002.
[49] International Organization for Standardization 2012, Rotodynamic pumps: Hydraulic performance acceptance tests: Grades 1, 2 and 3, ISO 9906:2012, International Organization for Standardization, Geneva.
[50] IEC 60193, Hydraulic turbines, storage pumps and pump turbines Model acceptance tests, (1999–2011).
[51] I. Farrance, T. Badrick, R. Frenkel, Uncertainty in measurement: A review of the procedures for determining uncertainty in measurement and its use in deriving the biological variation of the estimated glomerular filtration rate, Pract. Lab. Med. 12 (2018) 1–13. https://doi.org/10.1016/j.PLABM.2018.e00097.
[52] R.F. Dwyer, FRAM 2 Single Channel Ambient Noise Statistics. 101st Meeting of the Acoust. Soc. of Am. (1981).
[53] R.F. Dwyer, Detection of non-Gaussian signals by frequency domain kurtosis estimation, IEEE International Conference on Acoustics, Speech, and Signal Processing. 8(1983) 607-610. https://doi.org/10.1109/ICASSP.1983.1172264.
[54] R. F. Dwyer, A technique for improving detection and estimation of signals contaminated by under ice noise, The Journal of the Acoustical Society of America, 74(1983) 124-130. https://doi.org/10.1121/1.389729.
[55] R. F. Dwyer, Use of the kurtosis statistic in the frequency domain as an aid in detecting random signals. IEEE Journal of Oceanic Engineering, (1984) 85-92.
[56] R.B. Randall, J. Antoni, Rolling element bearing diagnostics-A tutorial, Mech. Syst. Signal Process. 25 (2011) 485–520. https://doi.org/10.1016/j.ymssp.2010.07.017.
[57] R. B. Randall, Vibration-based condition monitoring: industrial, aerospace and automotive applications, John Wiley & Sons, 2011.
[58] C.T. Yiakopoulos, K.C. Gryllias, I.A. Antoniadis, Rolling element bearing fault detection in industrial environments based on a K-means clustering approach, Expert Syst. Appl. 38 (2011) 2888–2911. https://doi.org/10.1016/j.eswa.2010.08.083.
[59] K.C. Gryllias, I.A. Antoniadis, A Support Vector Machine approach based on physical model training for rolling element bearing fault detection in industrial environments, Eng. Appl. Artif. Intell. 25 (2012) 326–344. https://doi.org/10.1016/j.engappai.2011.09.010.
[60] M. Chudina, Pumps and pumping system noise and vibration prediction and control, Handbook of Noise and Vibration Control, (2007) 897-909.
[61] H.H. Anderson, Centrifugal pumps and allied machinery, Elsevier, 1994.
[62] P.D. Welch, The Use of Fast Fourier Transform for the Estimation of Power Spectra: A Method Based on Time Averaging Over Short, Modified Periodograms, IEEE Trans. Audio Electroacoust. 15 (1967) 70–73. https://doi.org/10.1109/TAU.1967.1161901.
[63] J.I. Taylor, The vibration analysis handbook, 2005.

[64] C. Scheffer, Pump condition monitoring through vibration analysis, In Pumps: Maintenance, Design, and Reliability Conference, (2008) 1135-1146.
[65] R. B. Randall, Noise and vibration data analysis. Handbook of Noise and Vibration Control, John Wiley & Sons, 2007.
[66] X. Zhang, J. Kang, L. Xiao, J. Zhao, H. Teng, A new improved Kurtogram and its application to bearing fault diagnosis, Shock Vib. 2015 (2015). https://doi.org/10.1155/2015/385412.
[67] L. Li, M. Li, F. Chen, A Fast Kurtogram Demodulation Method in Rolling Bearing Fault Diagnosis, MATEC Web Conf. 77 (2016) 0–3. https://doi.org/10.1051/matecconf/20167701003.
[68] J. Antoni, R.B. Randall, The spectral kurtosis: Application to the vibratory surveillance and diagnostics of rotating machines, Mech. Syst. Signal Process. 20 (2006) 308–331. https://doi.org/10.1016/j.ymssp.2004.09.002.
[69] N. Sawalhi, R.B. Randall, Spectral kurtosis optimization for rolling element bearings, Proc. - 8th Int. Symp. Signal Process. Its Appl. ISSPA 2005. 2 (2005) 839–842. https://doi.org/10.1109/ISSPA.2005.1581069.

Figure 1

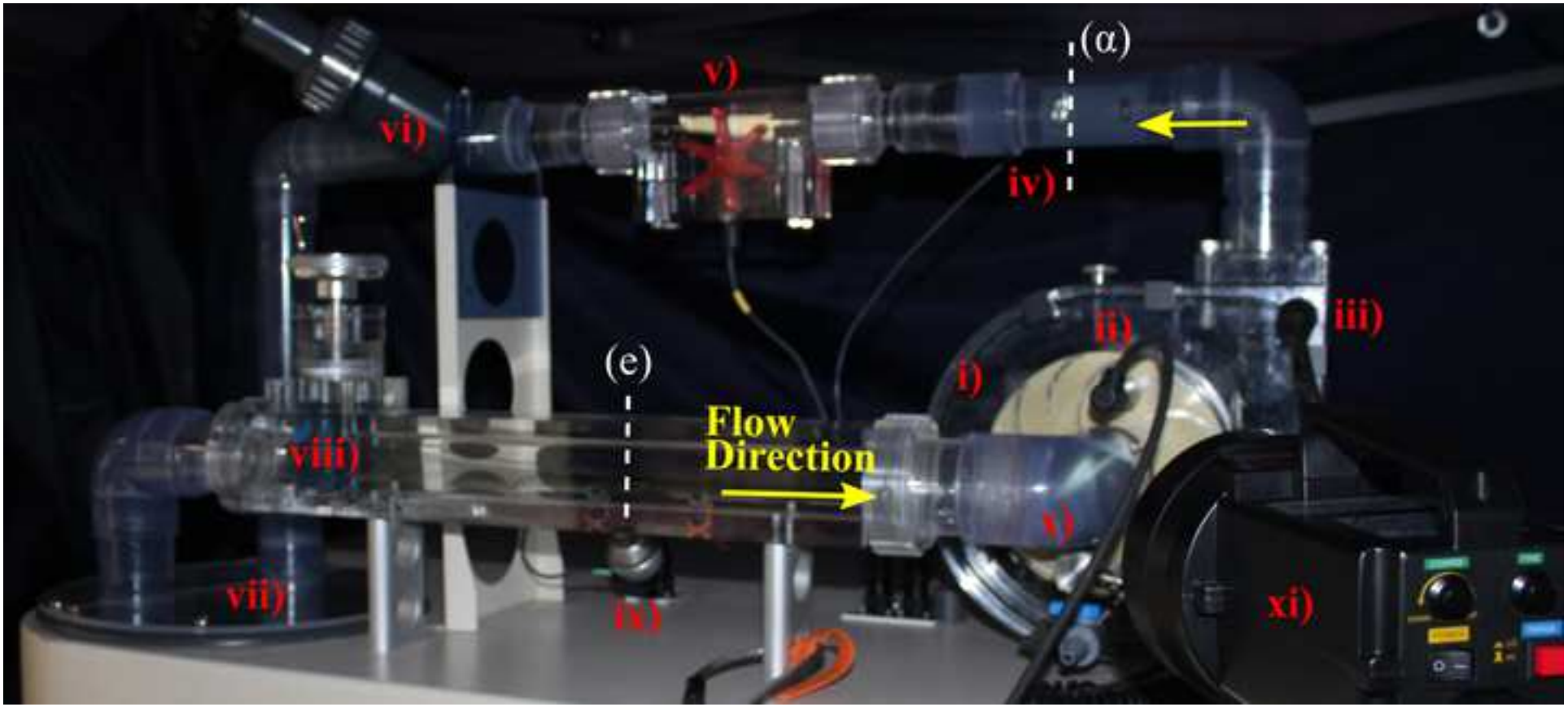

Figure 2

Click here to access/download;Figure;2.tif

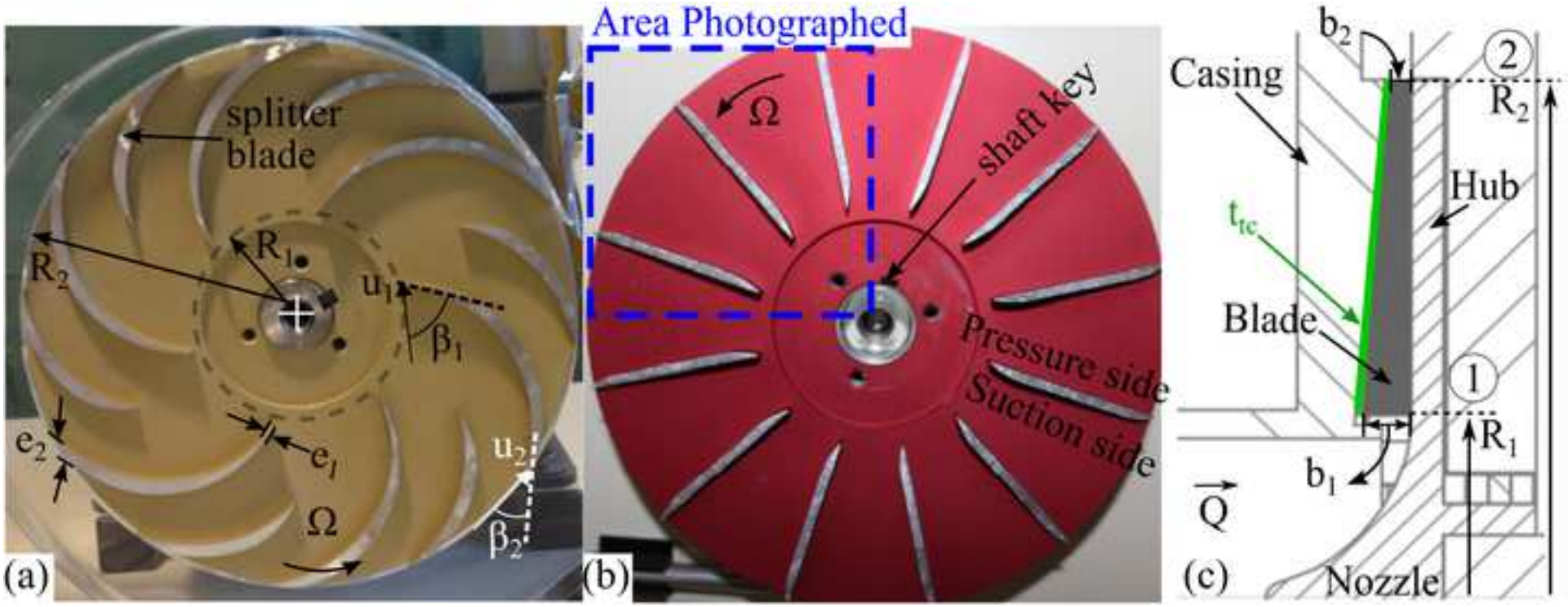

Figure 3

Click here to access/download;Figure;3.tif

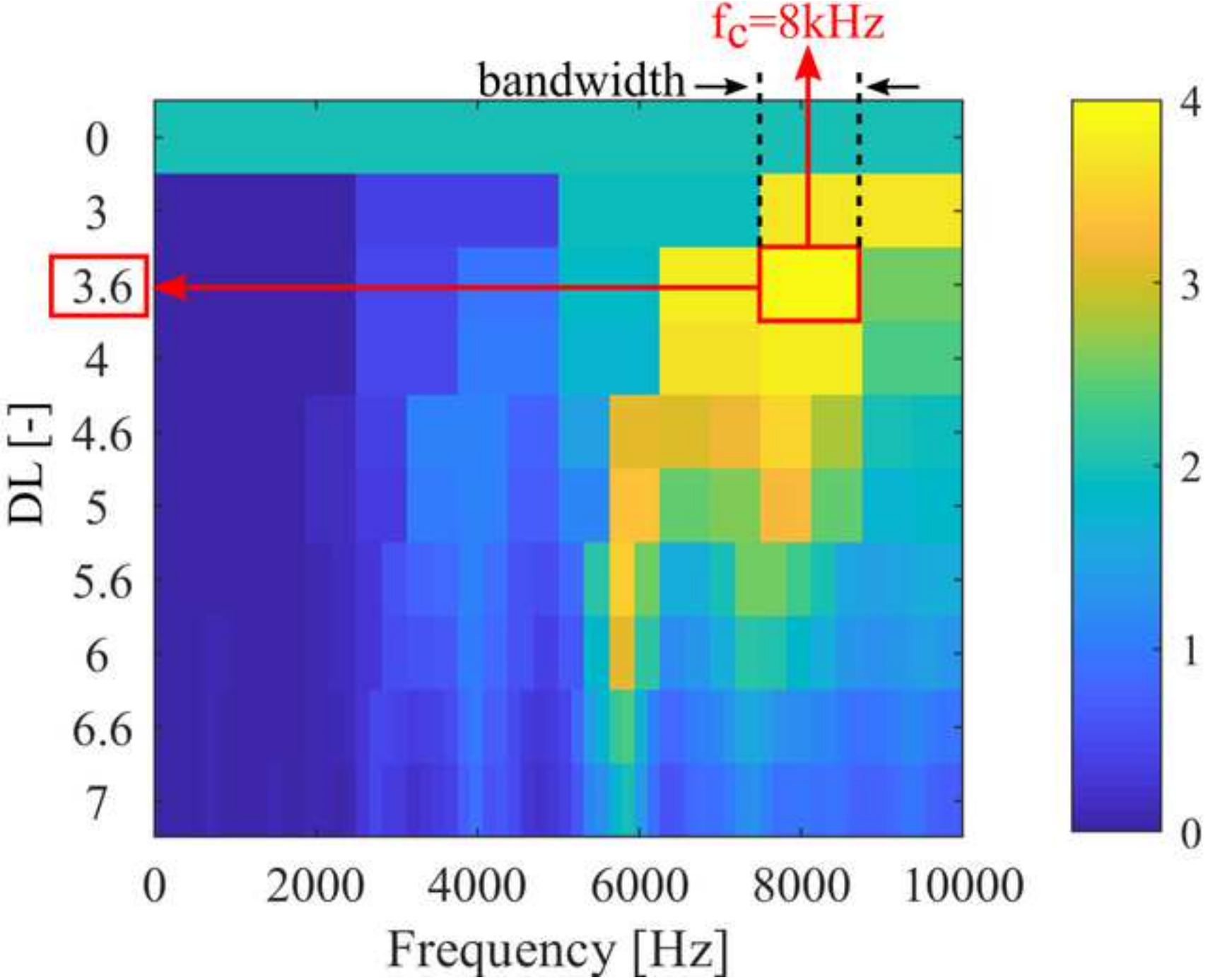

Figure 4a

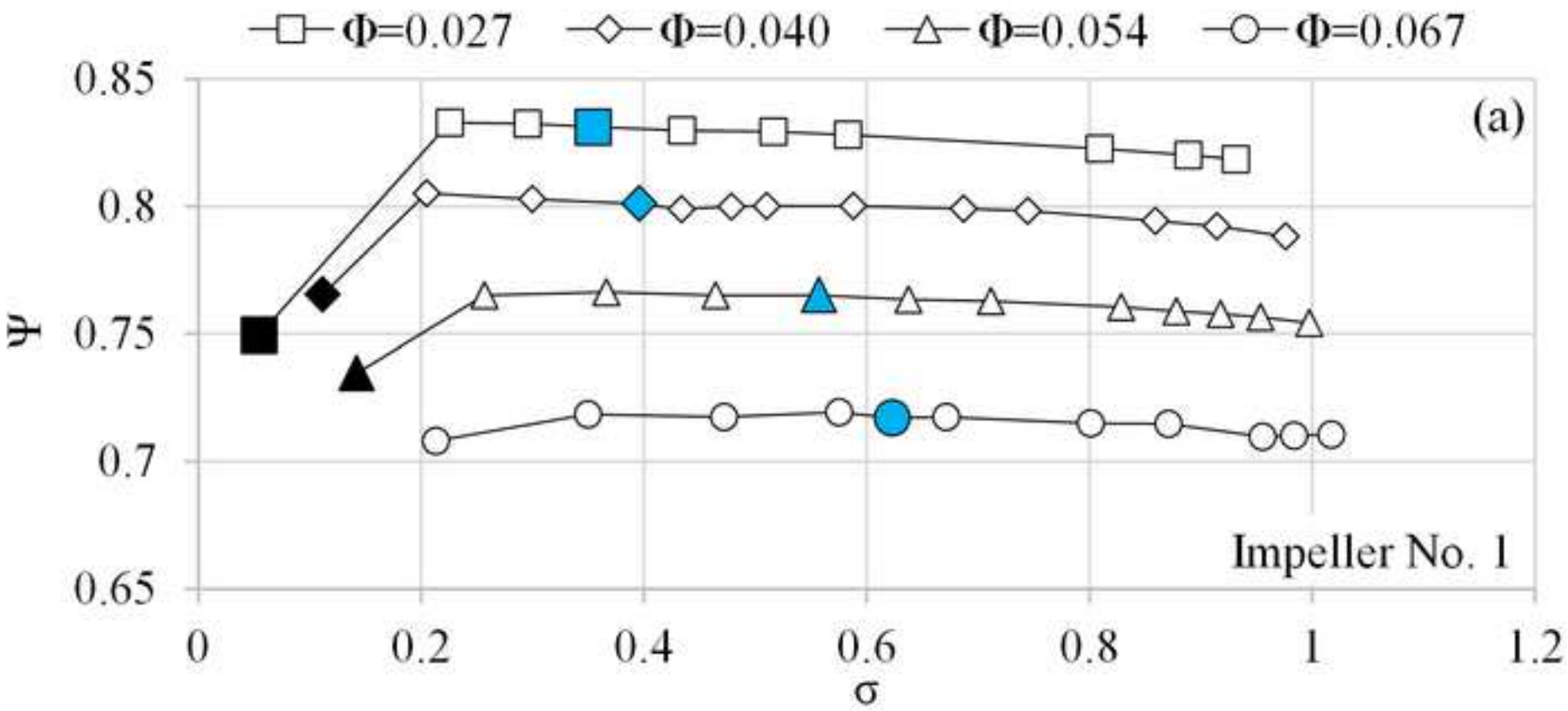

Figure 4b

Click here to access/download;Figure;4b.tif

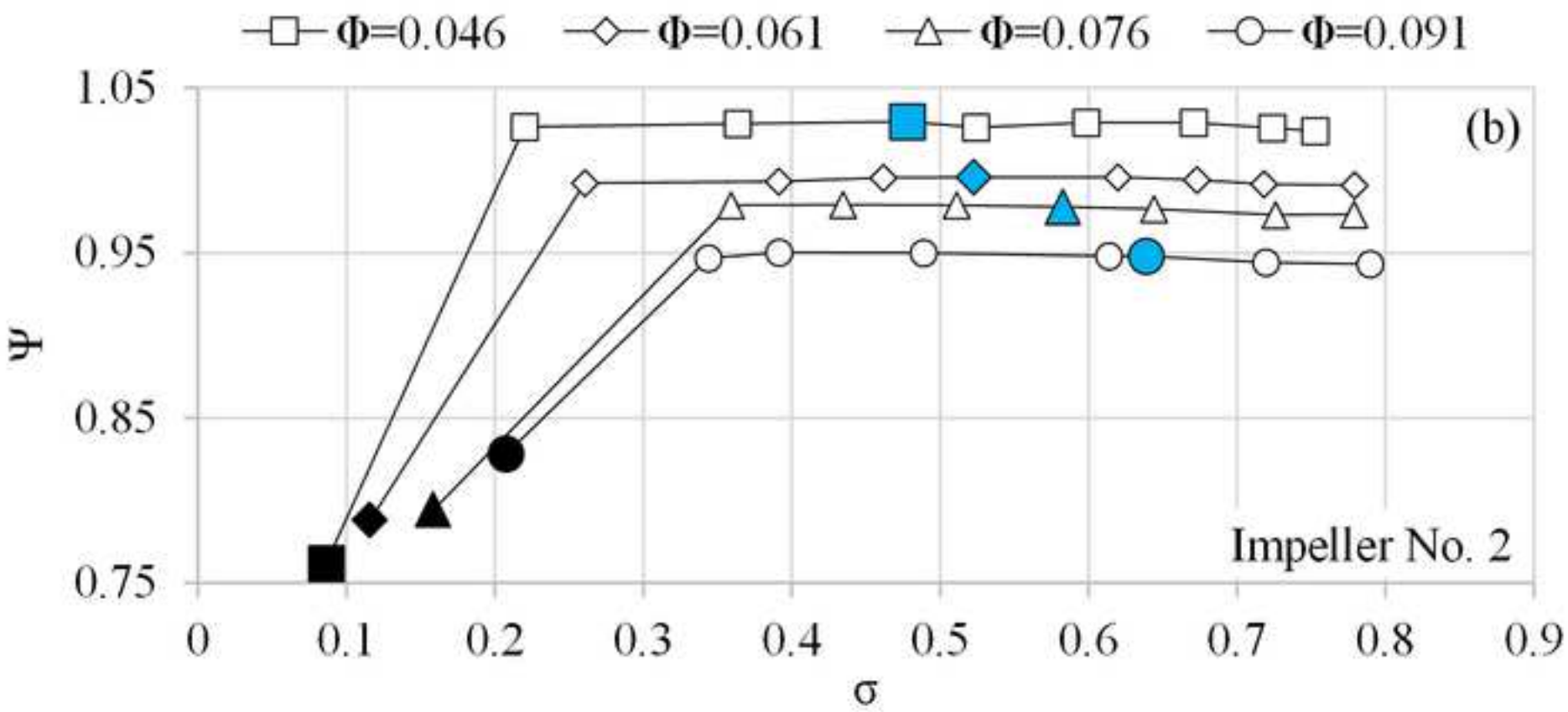

Figure 5

Click here to access/download;Figure;5.tif

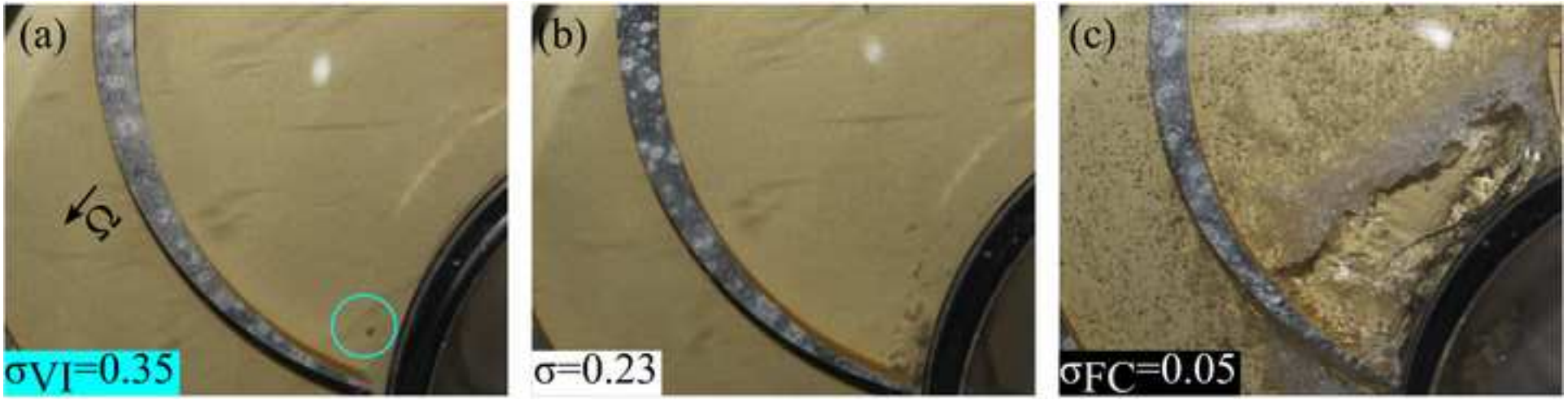

Figure 6

Figure 7a

Click here to access/download;Figure;7a.tif

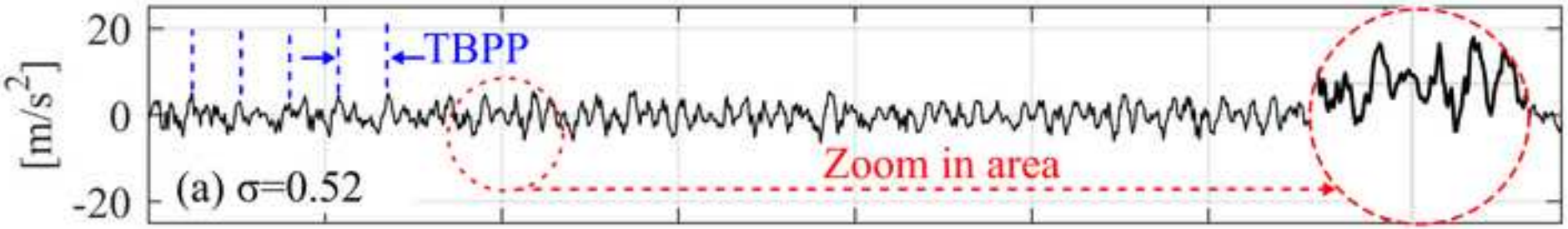

Figure 7b

Click here to access/download;Figure;7b.tif

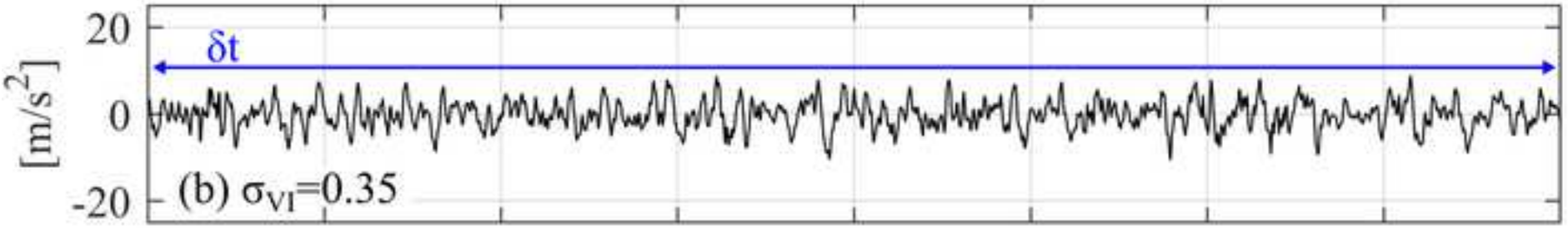

Figure 7c

Click here to access/download;Figure;7c.tif

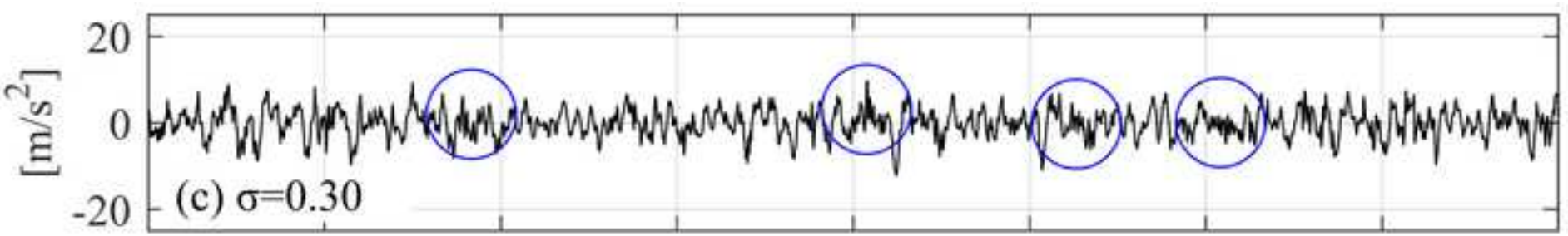

Figure 7d

Click here to access/download;Figure;7d.tif

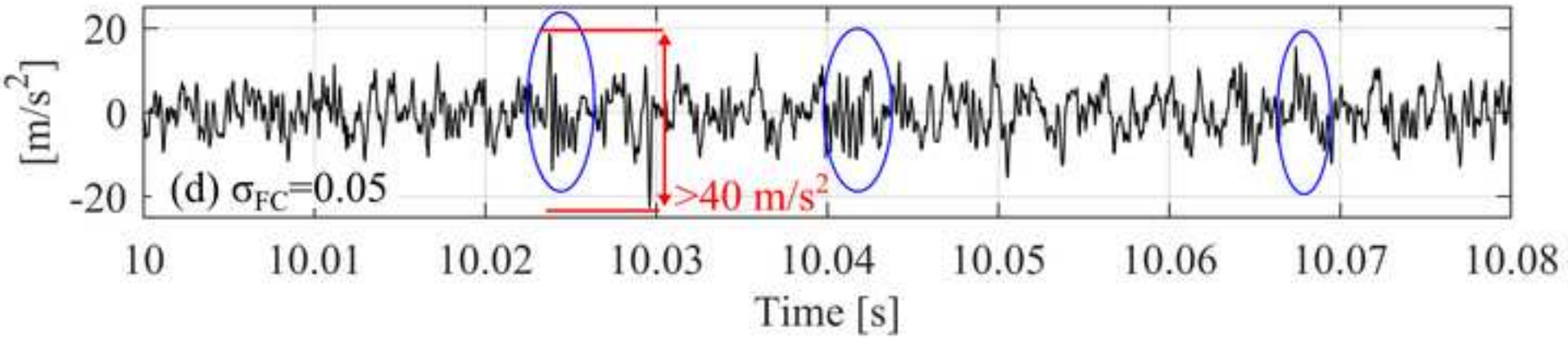

Figure 8a

Click here to access/download;Figure;8a.tif

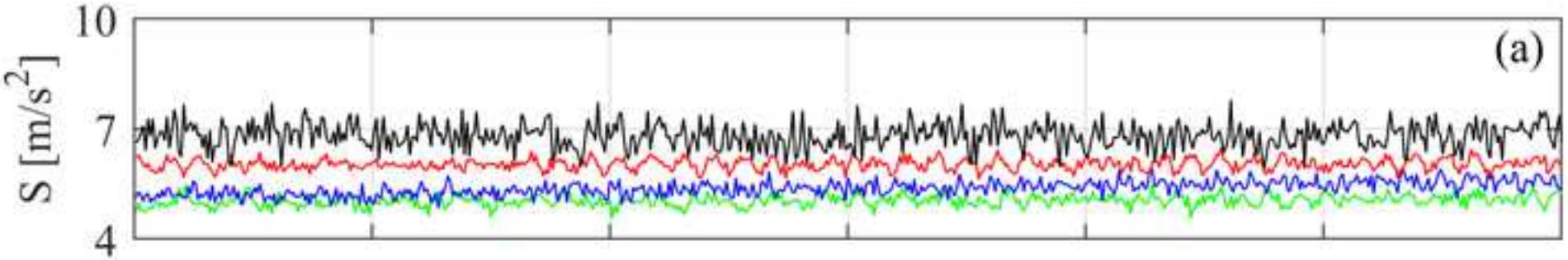

Figure 8b

Click here to access/download;Figure;8b.tif

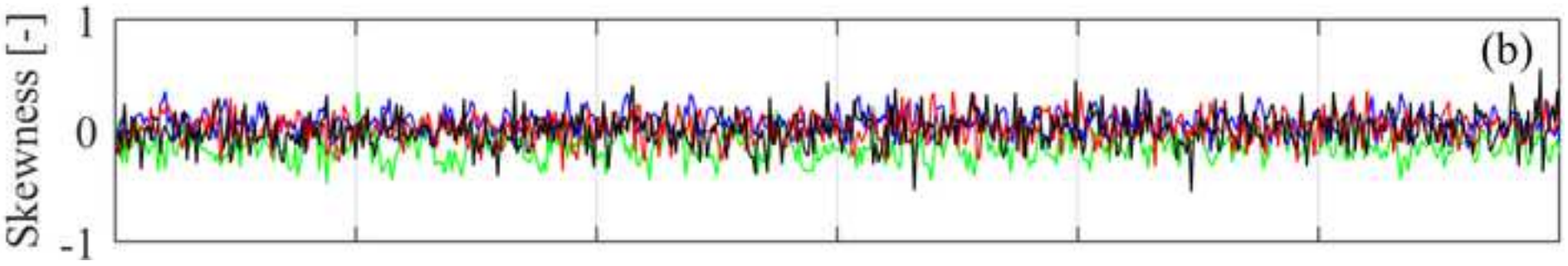

Figure 8c

Click here to access/download;Figure;8c.tif

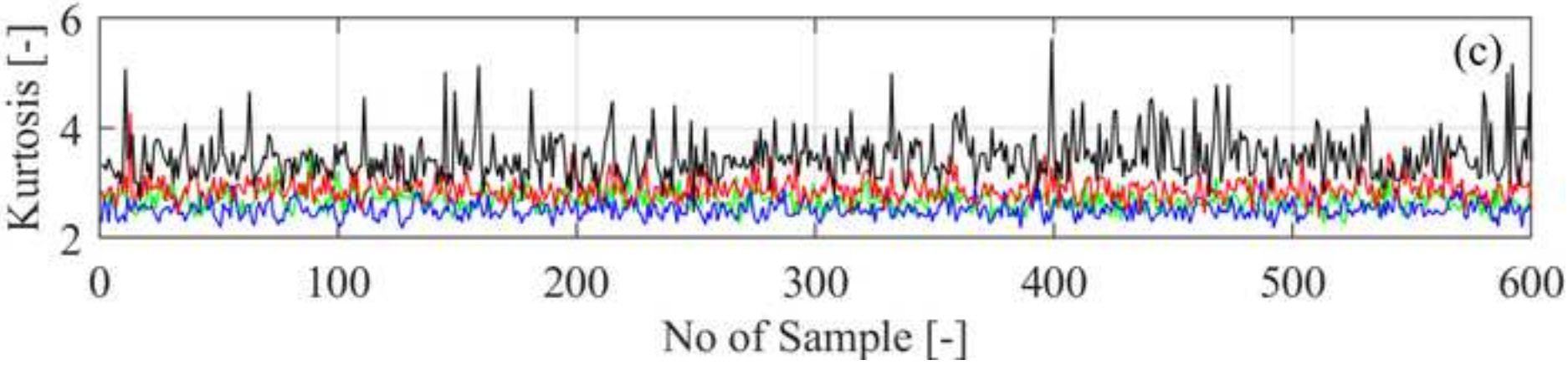

Figure 8-leg

Click here to access/download;Figure;8-legend.tif

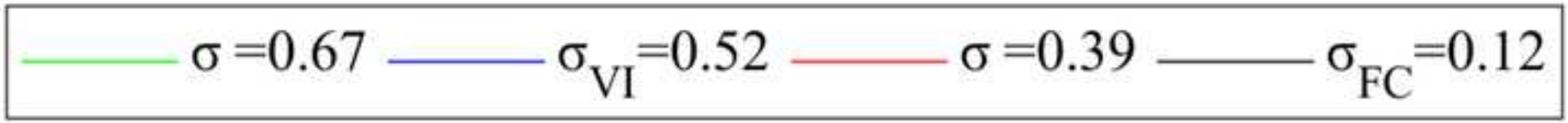

Figure 9a

Click here to access/download;Figure;9a.tif

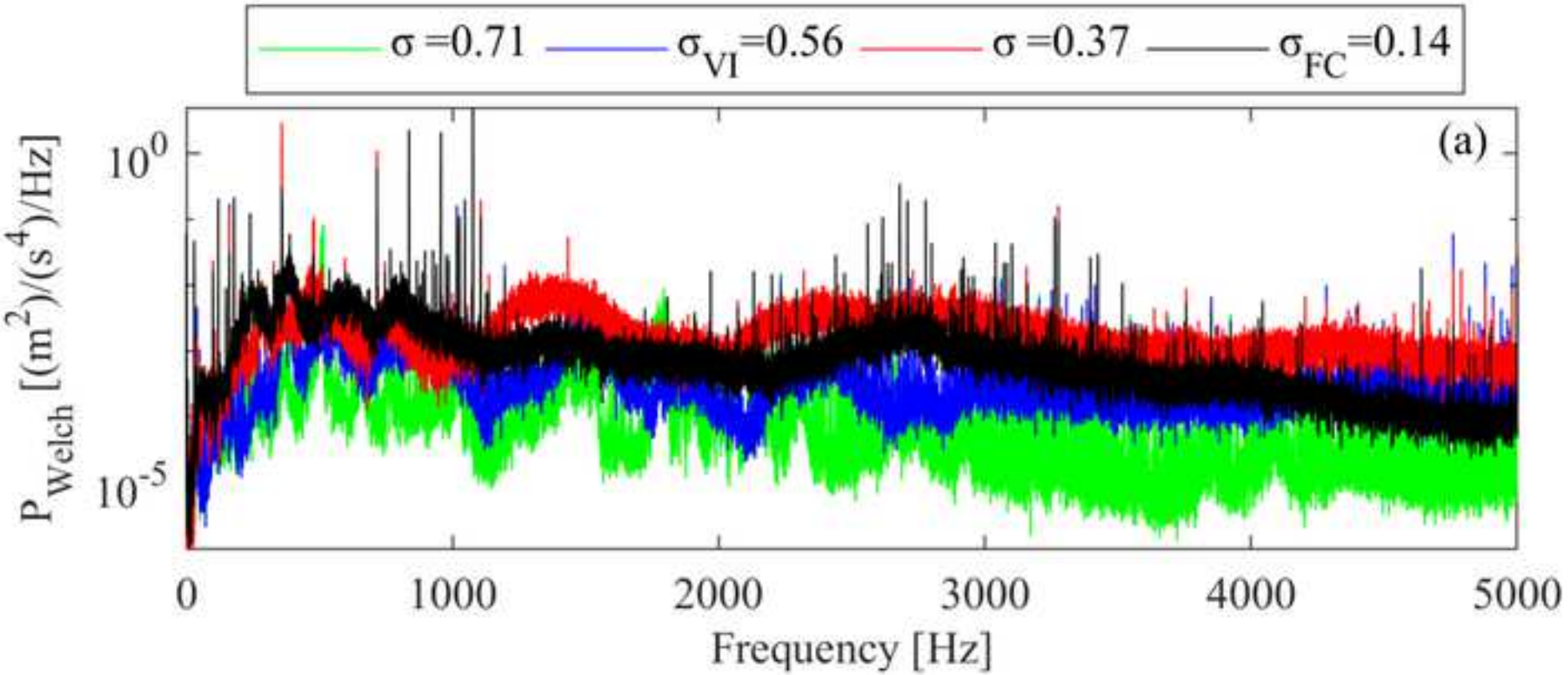

Figure 9b

Click here to access/download;Figure;9b.tif

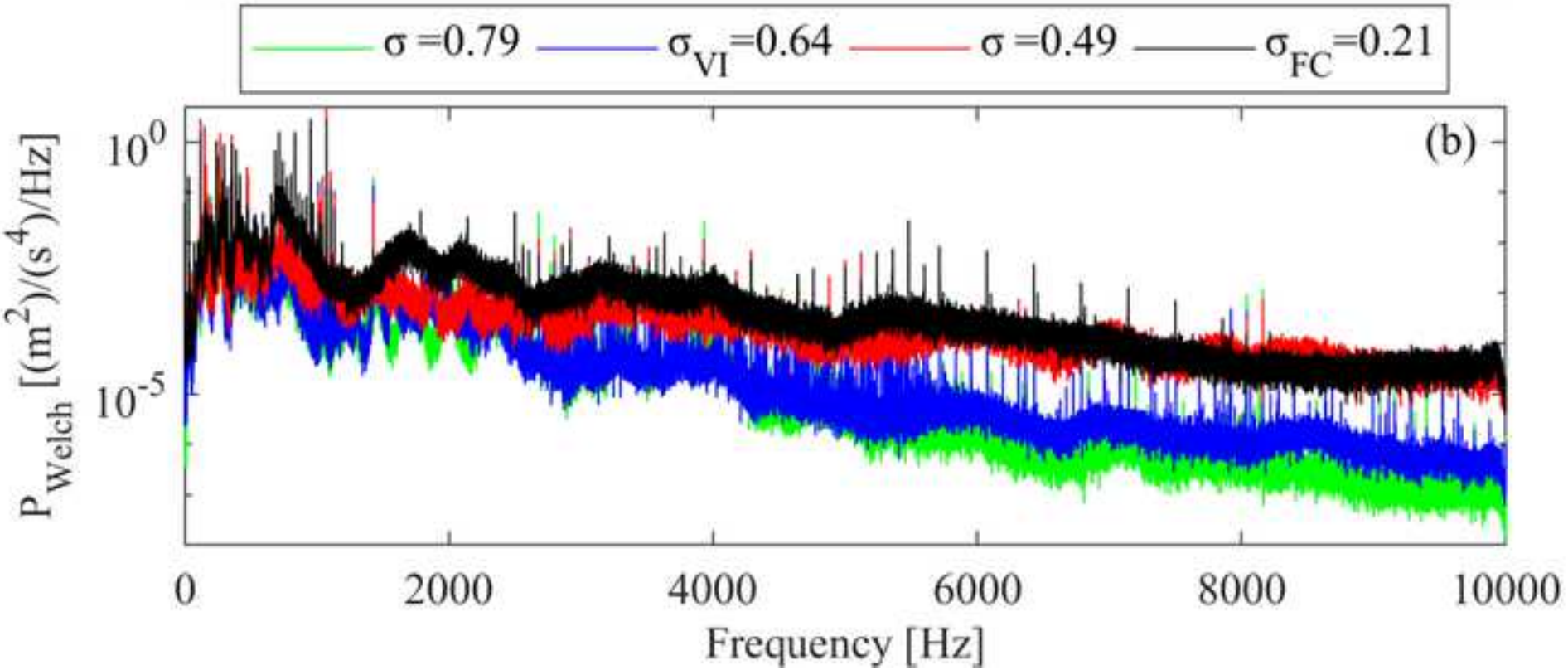

Figure 10a

Click here to access/download;Figure;10a.tif

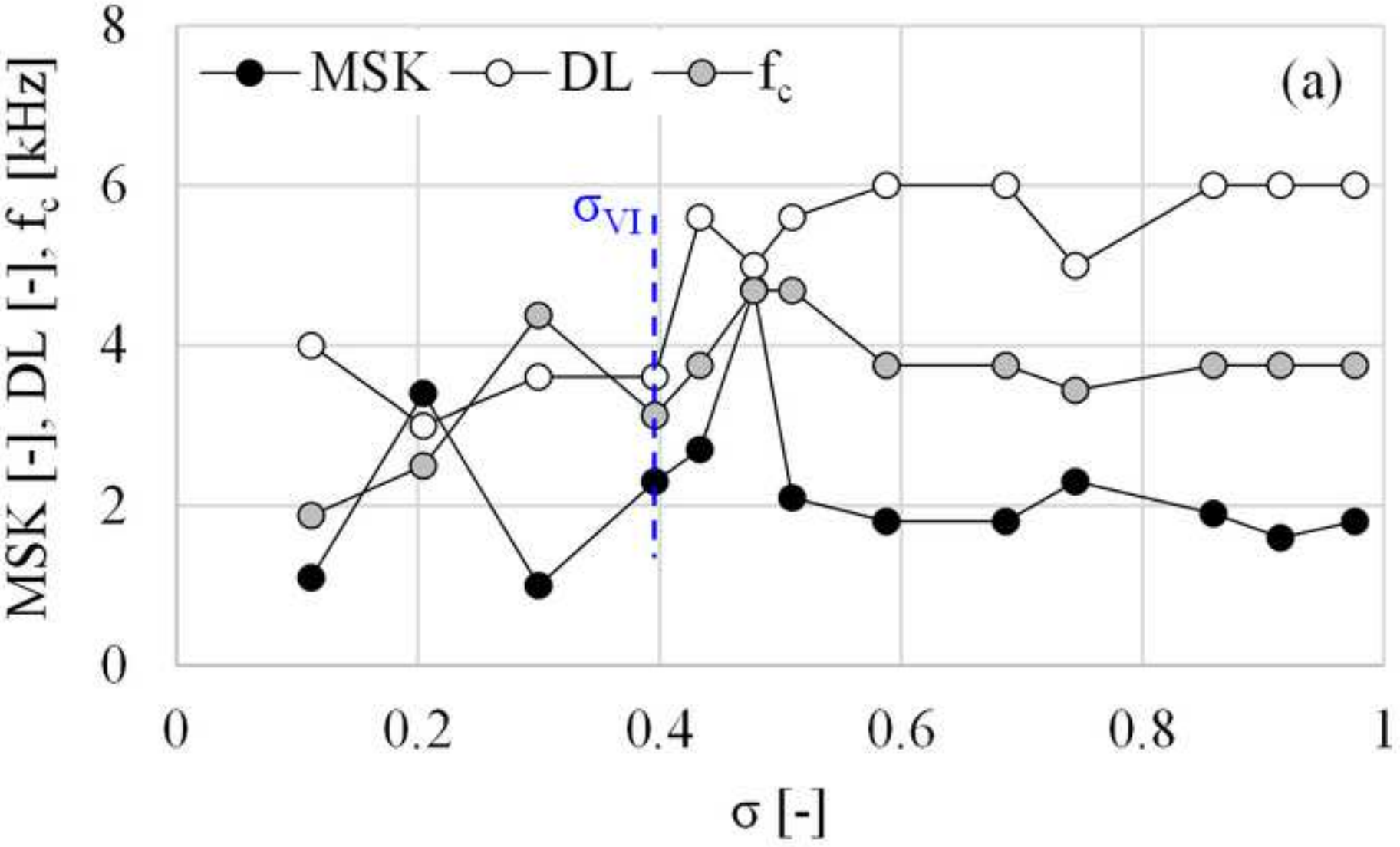

Figure 10b

Click here to access/download;Figure;10b.tif

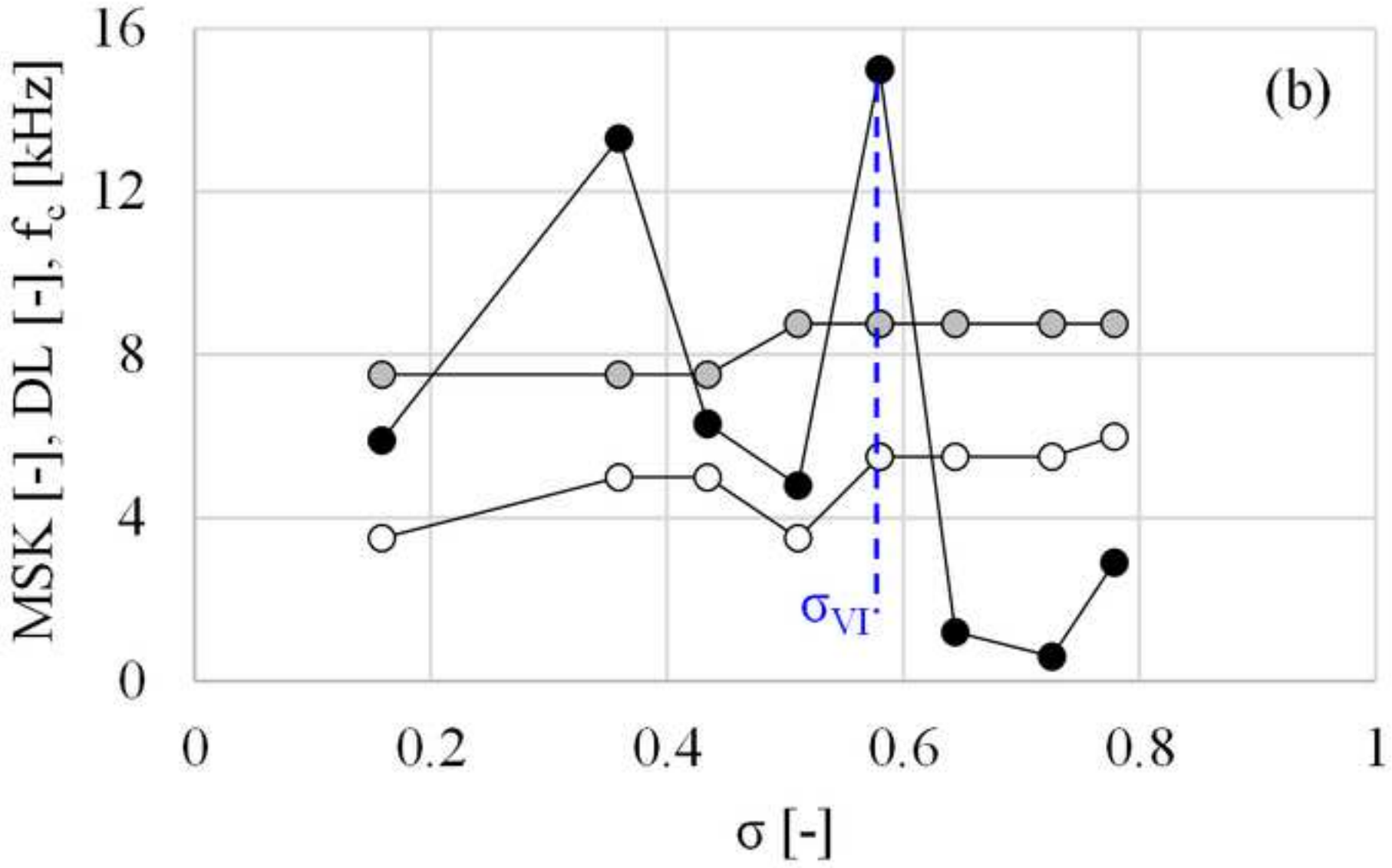

Figure 11a

Click here to access/download;Figure;11a.tif

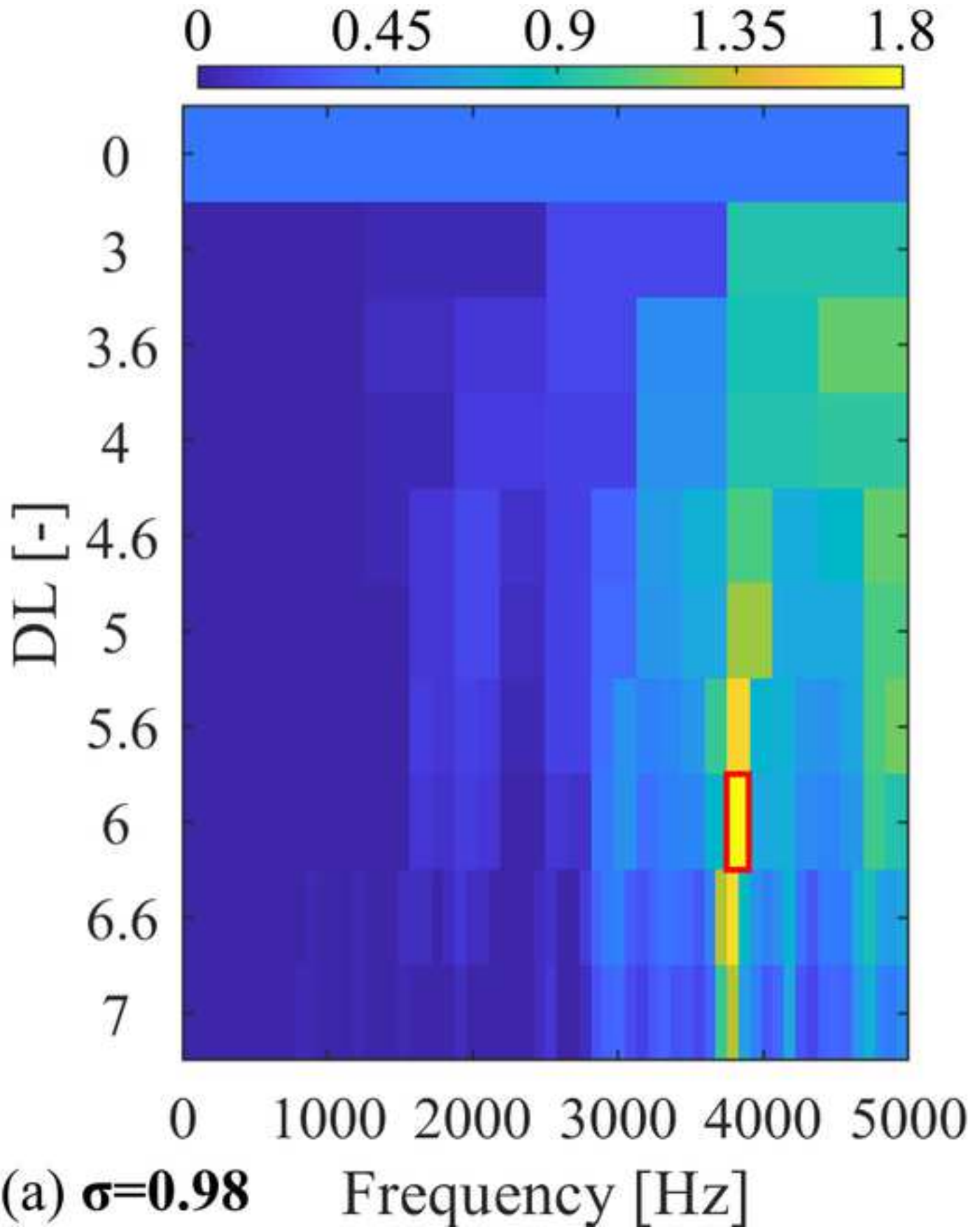

(a) **σ=0.98**

Figure 11b

Click here to access/download;Figure;11b.tif

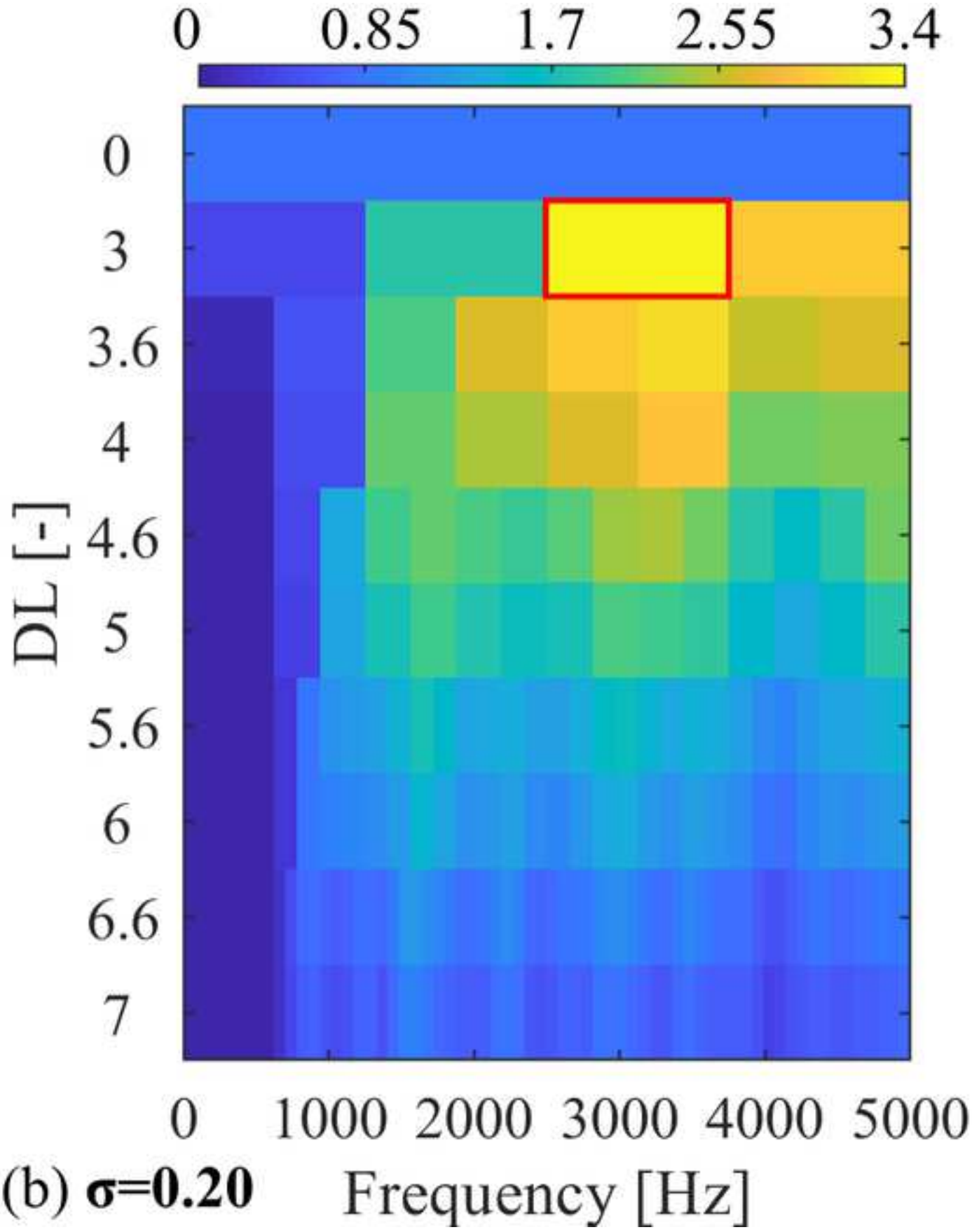

(b) **σ=0.20**

Figure 11c

Click here to access/download;Figure;11c.tif

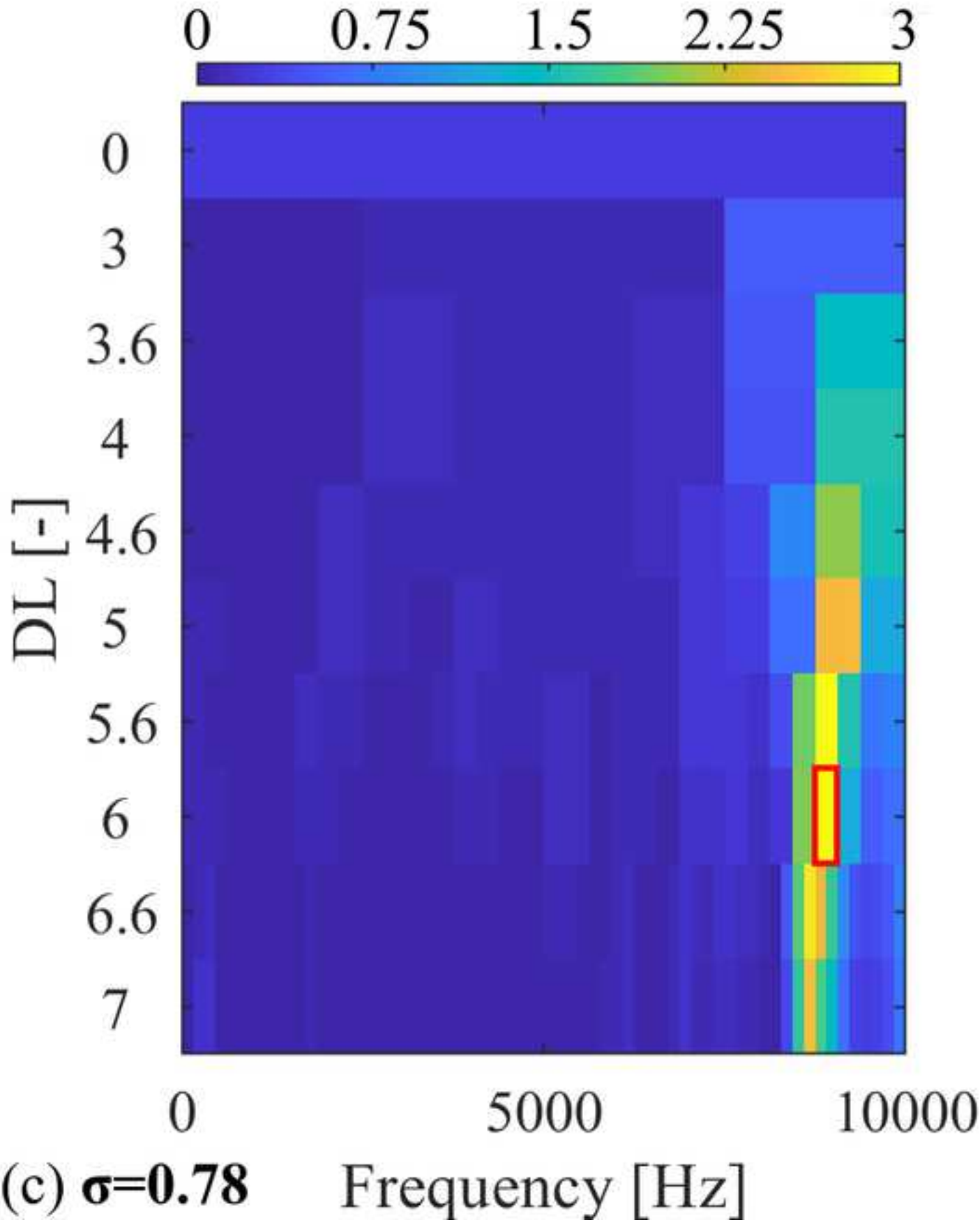

(c) **σ=0.78**

Figure 11d

Click here to access/download;Figure;11d.tif

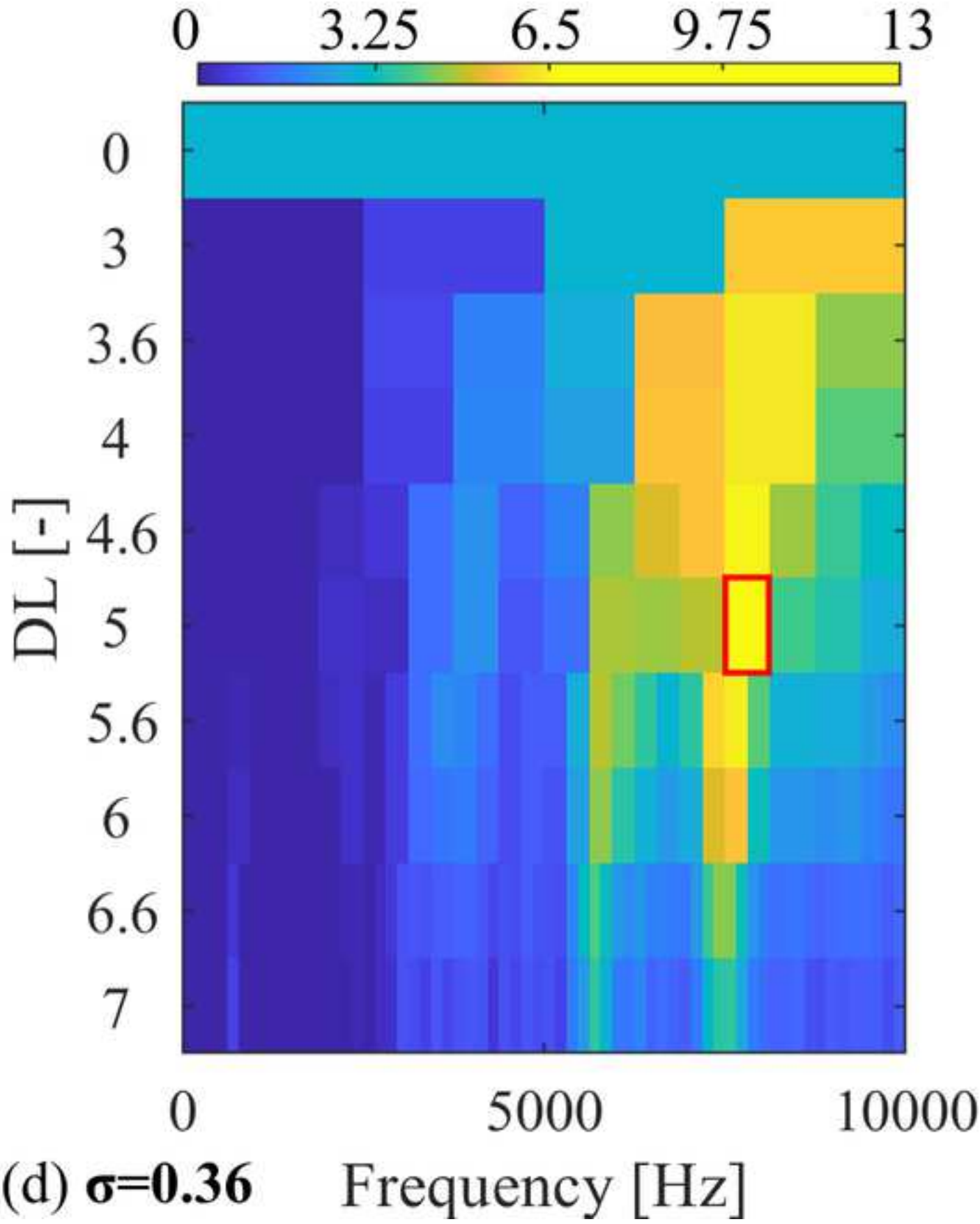

(d) **σ=0.36**

Figure 12a

Click here to access/download;Figure;12a.tif

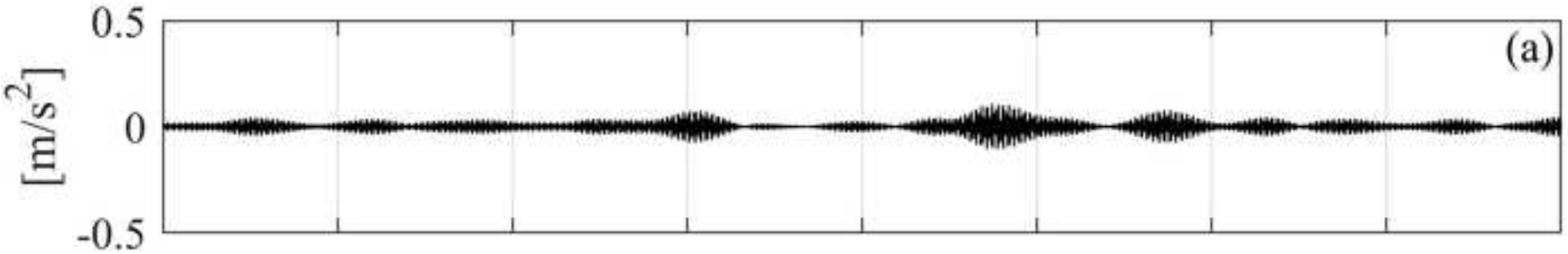

Figure 12b

Click here to access/download;Figure;12b.tif

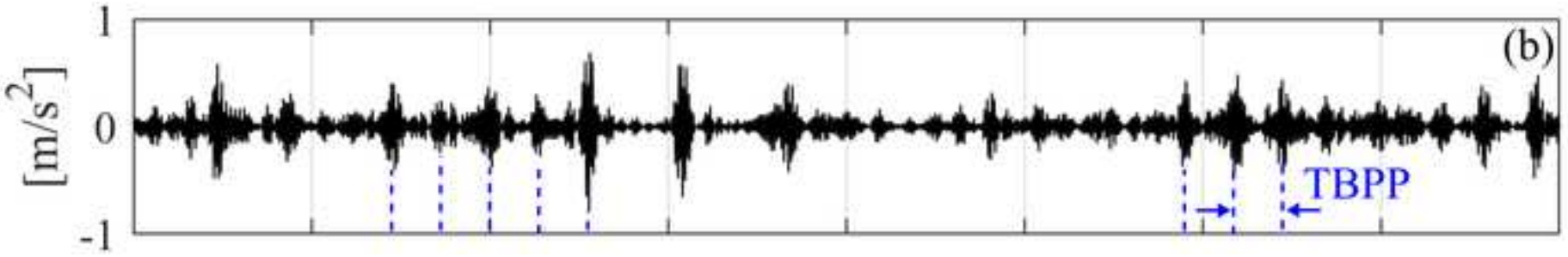

Figure 12c

Click here to access/download;Figure;12c.tif

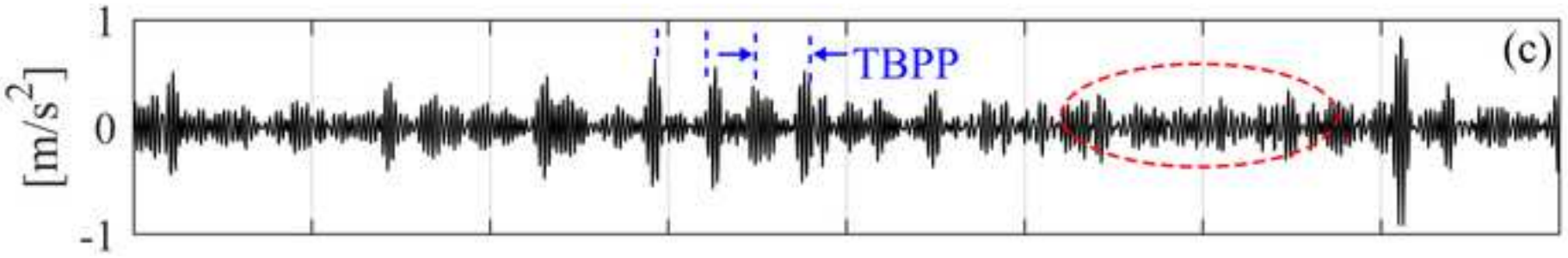

Figure 12d

Click here to access/download;Figure;12d.tif

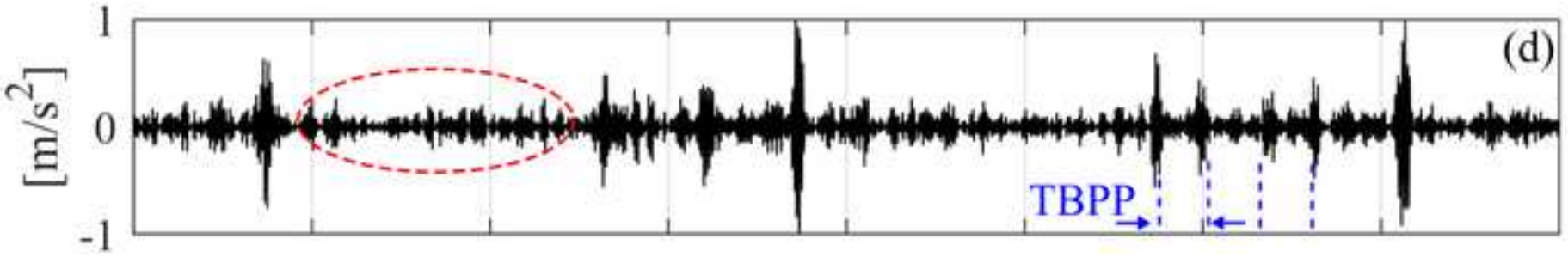

Figure 12e

Click here to access/download;Figure;12e.tif

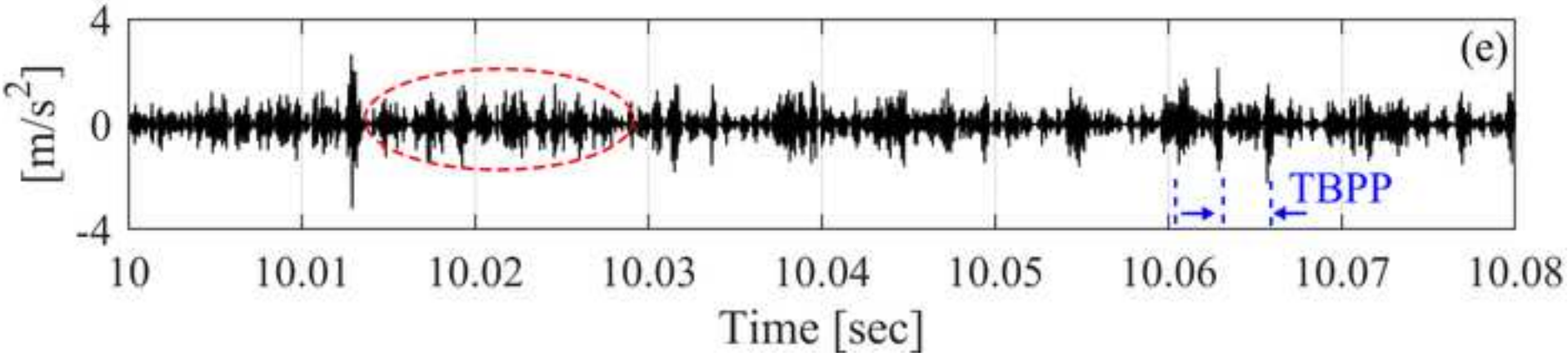

Figure 13a

Click here to access/download;Figure;13a.tif

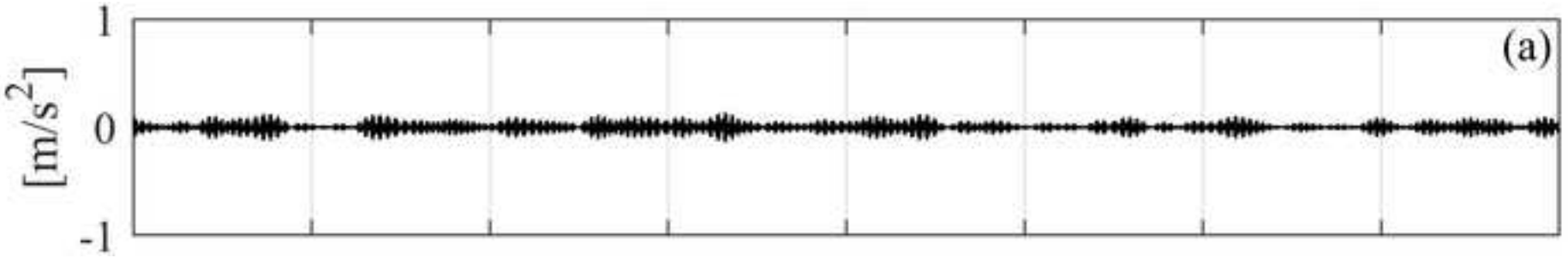

Figure 13b

Click here to access/download;Figure;13b.tif

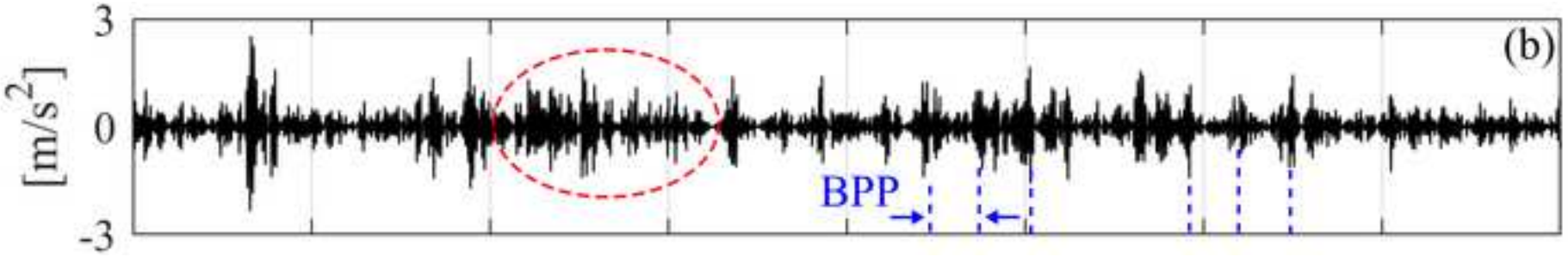

Figure 13c

Click here to access/download;Figure;13c.tif

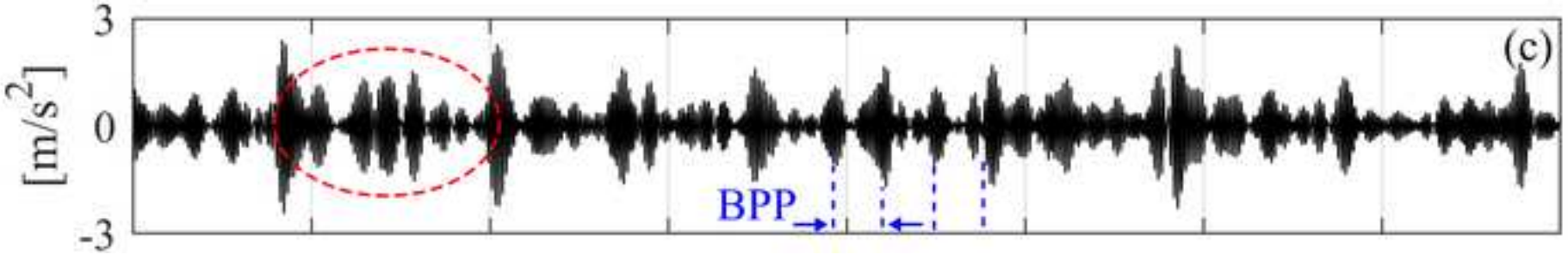

Figure 13d

Click here to access/download;Figure;13d.tif

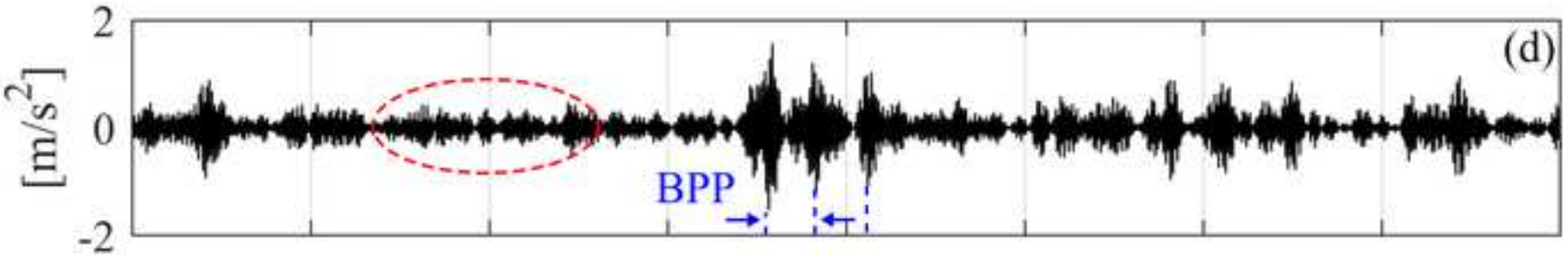

Figure 13e

Click here to access/download;Figure;13e.tif

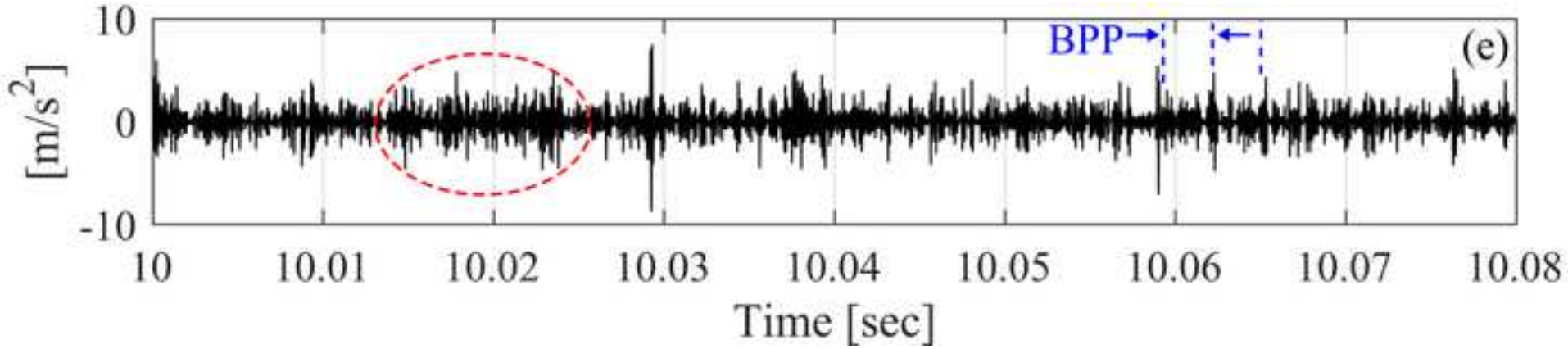

Figure 14a

Click here to access/download;Figure;14a.tif

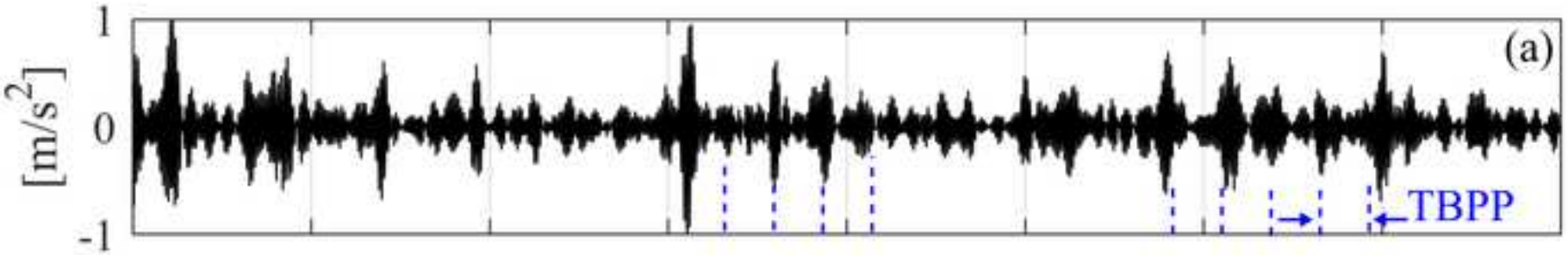

Figure 14b

Click here to access/download;Figure;14b.tif

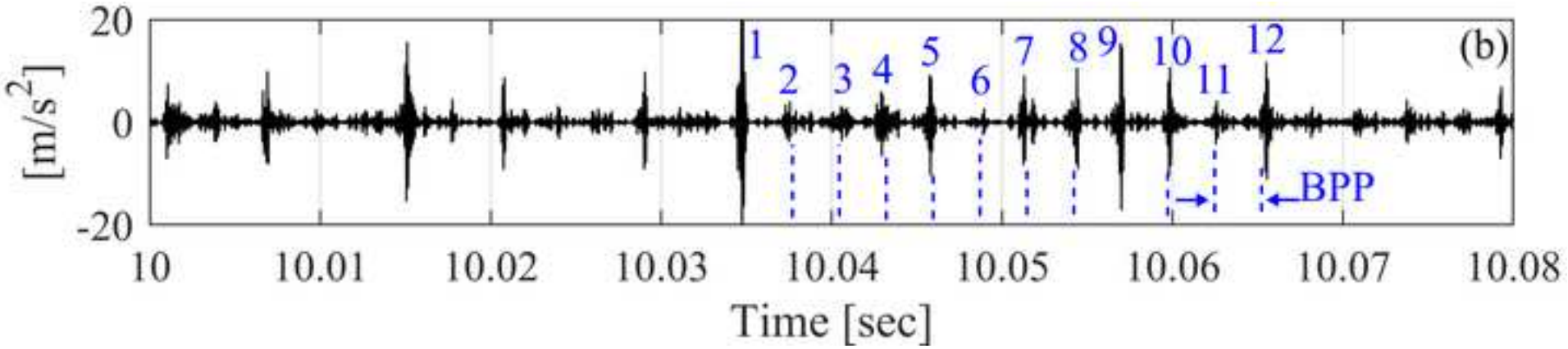

Figure 15a

Click here to access/download;Figure;15a.tif

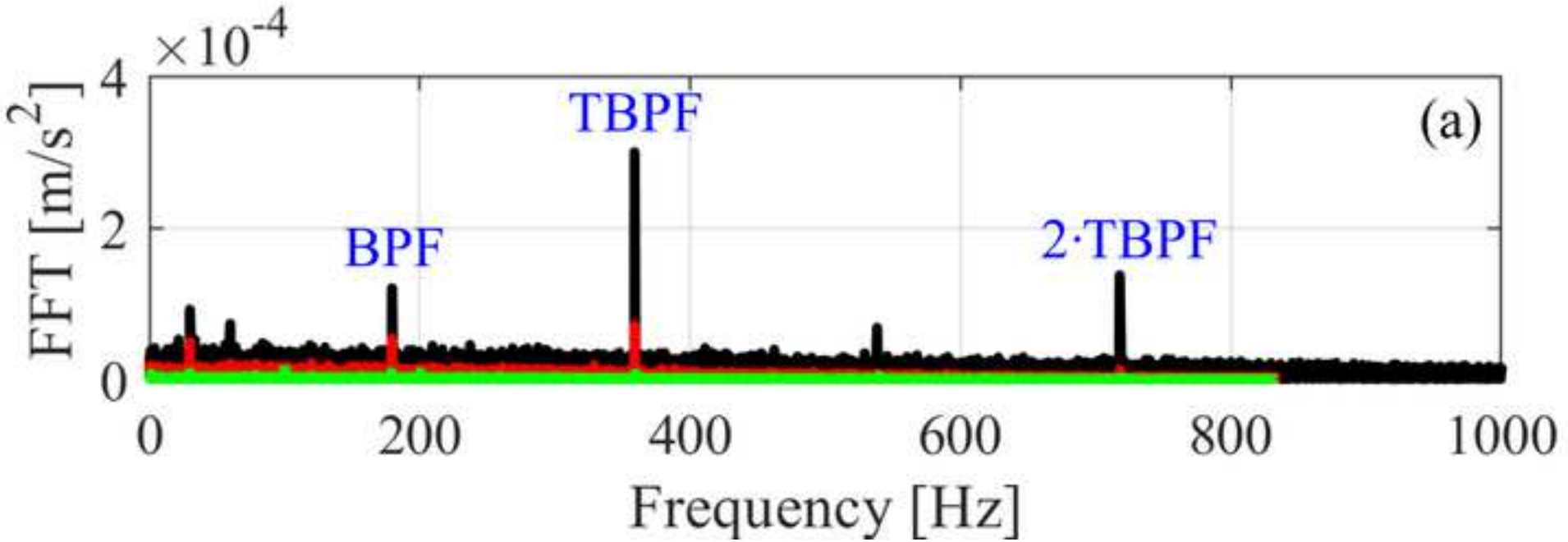

Figure 15b

Click here to access/download;Figure;15b.tif

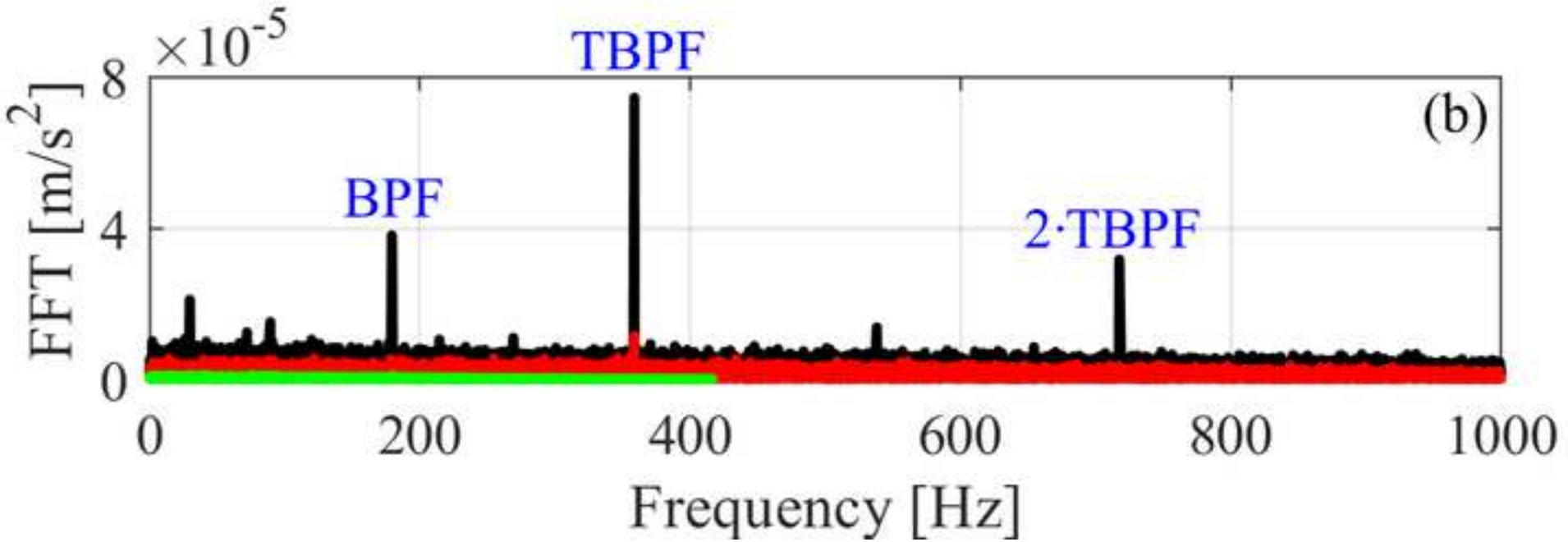

Figure 15c

Click here to access/download;Figure;15c.tif

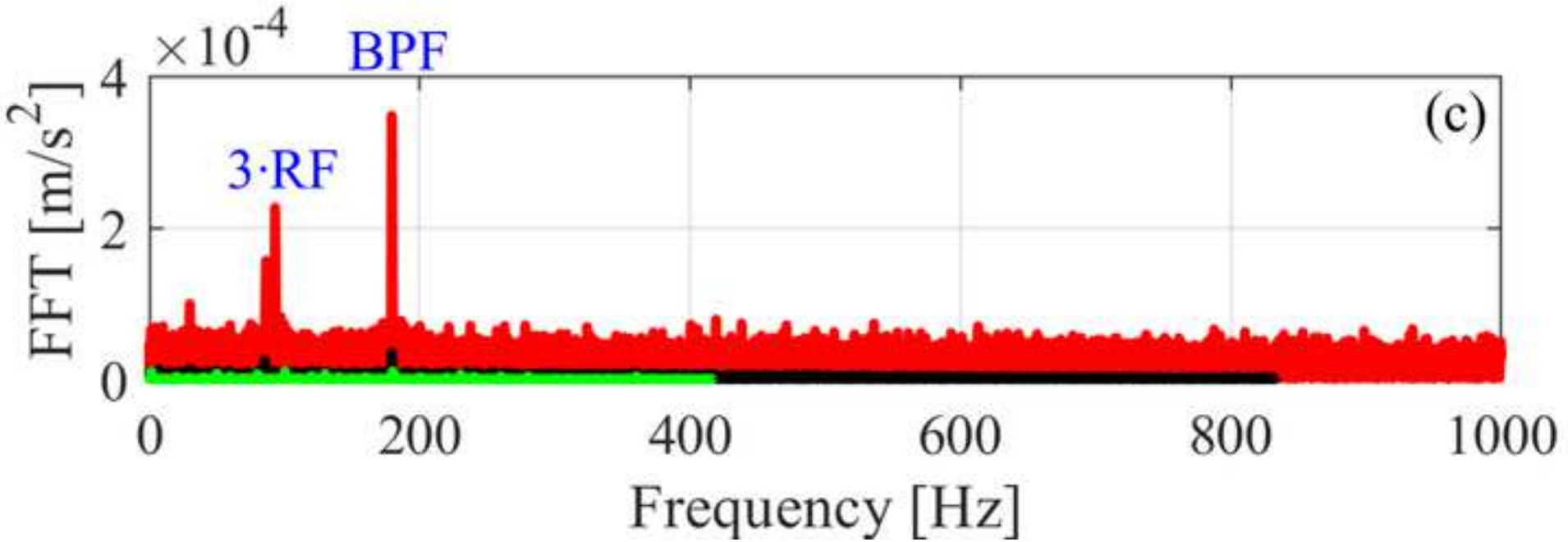

Figure 15d

Click here to access/download;Figure;15d.tif

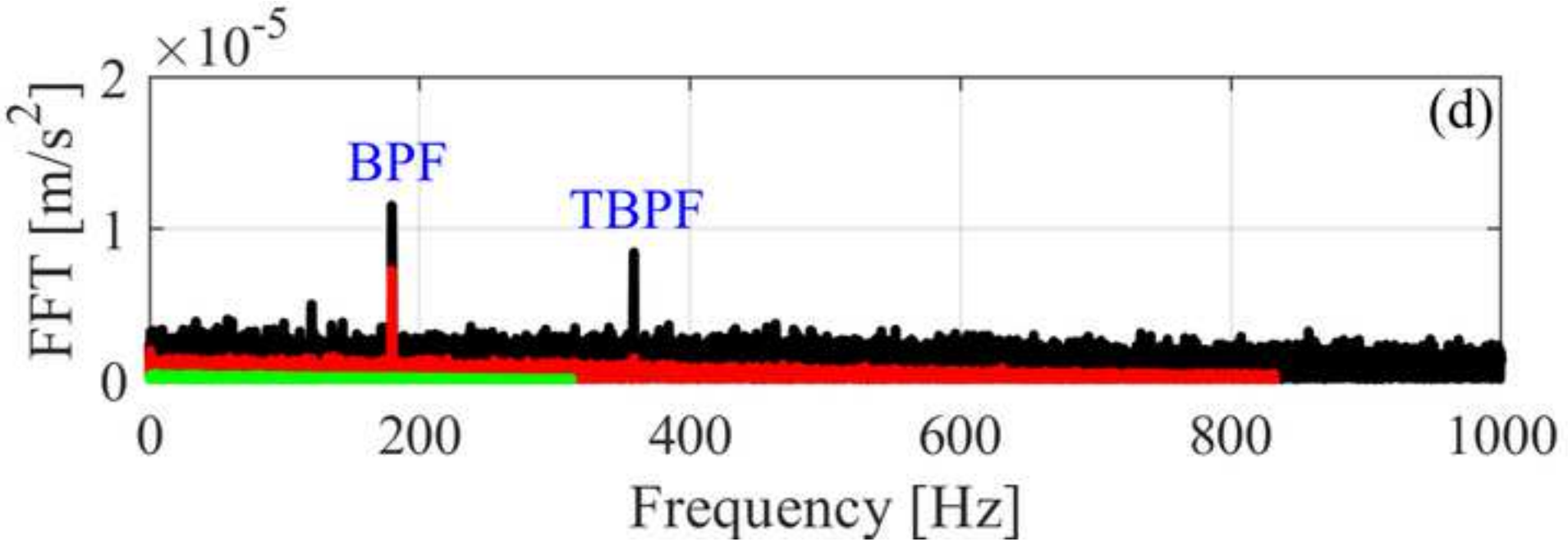

Figure 16a

Click here to access/download;Figure;16a.tif

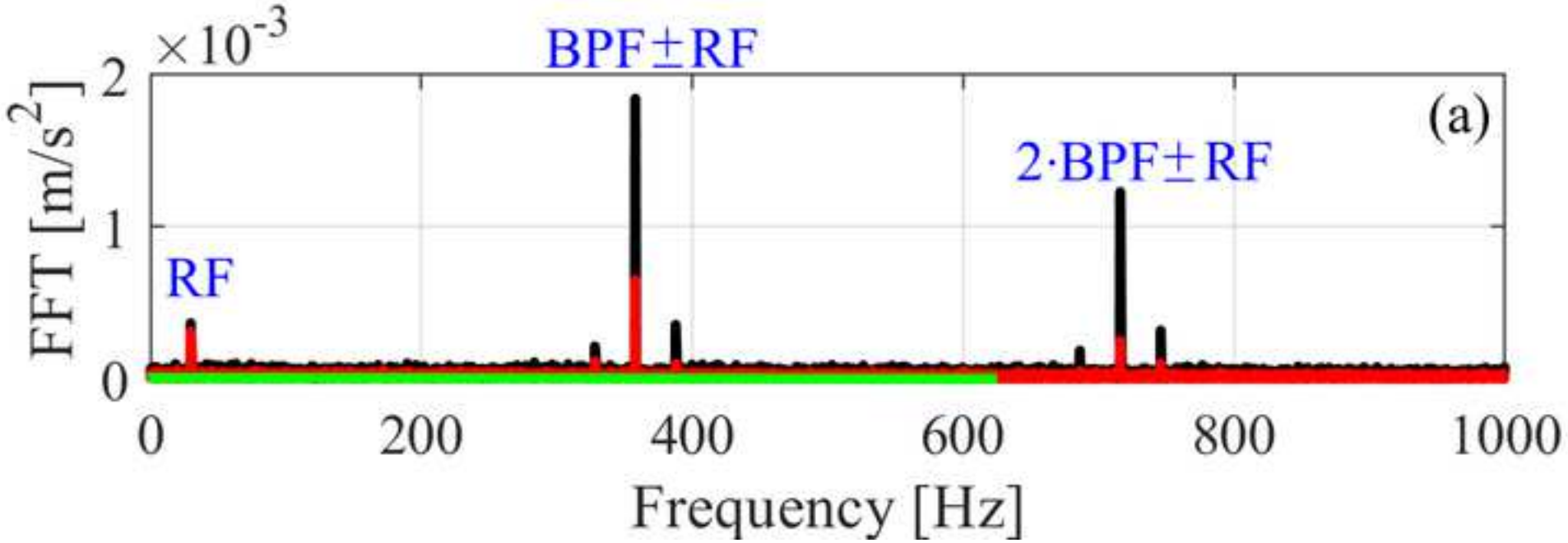

Figure 16b

Click here to access/download;Figure;16b.tif

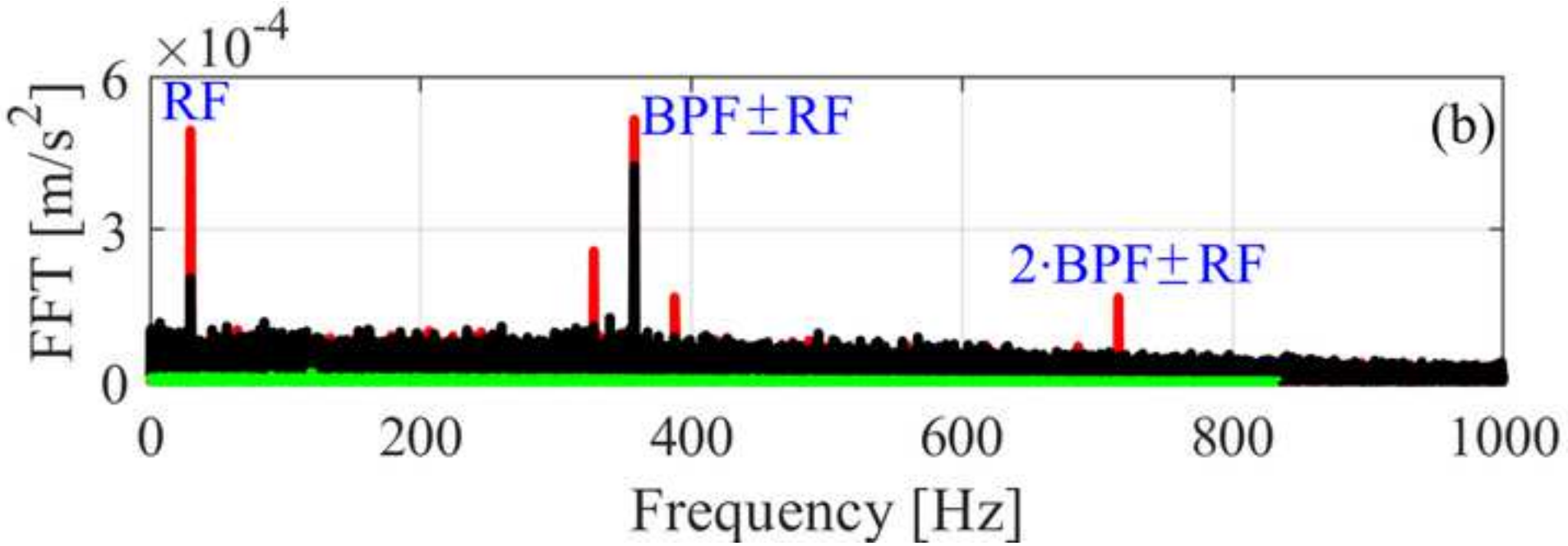

Figure 16c

Click here to access/download;Figure;16c.tif

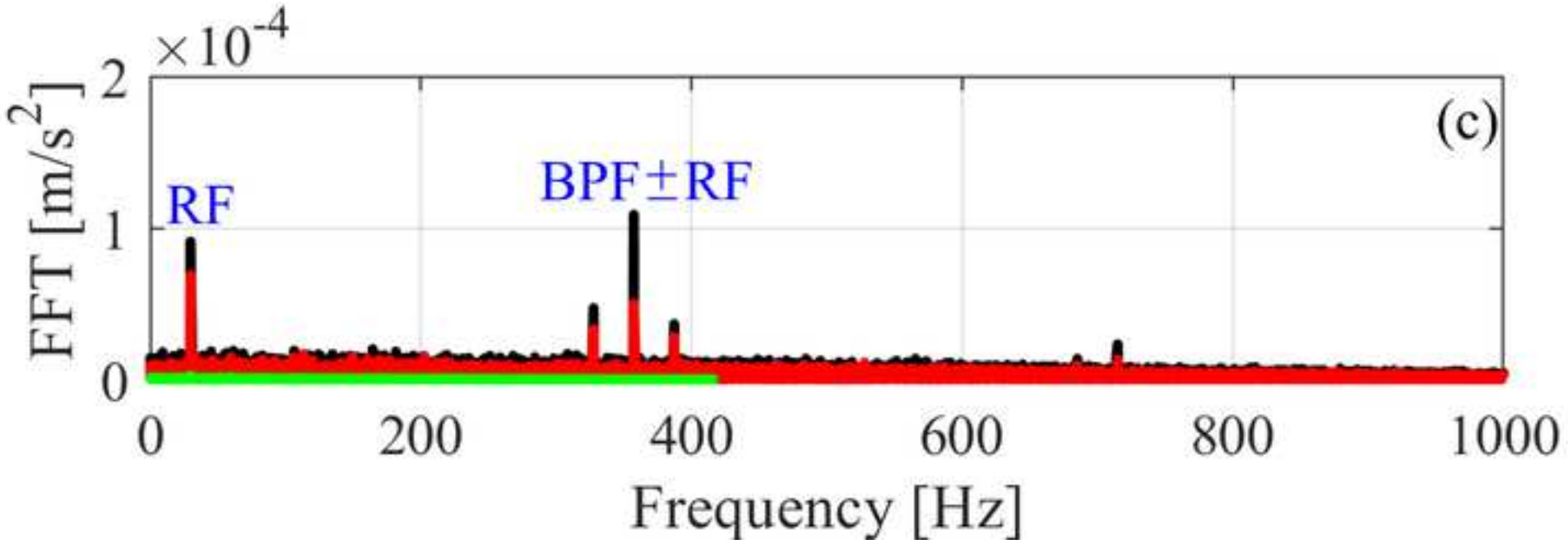

Figure 16d

Click here to access/download;Figure;16d.tif

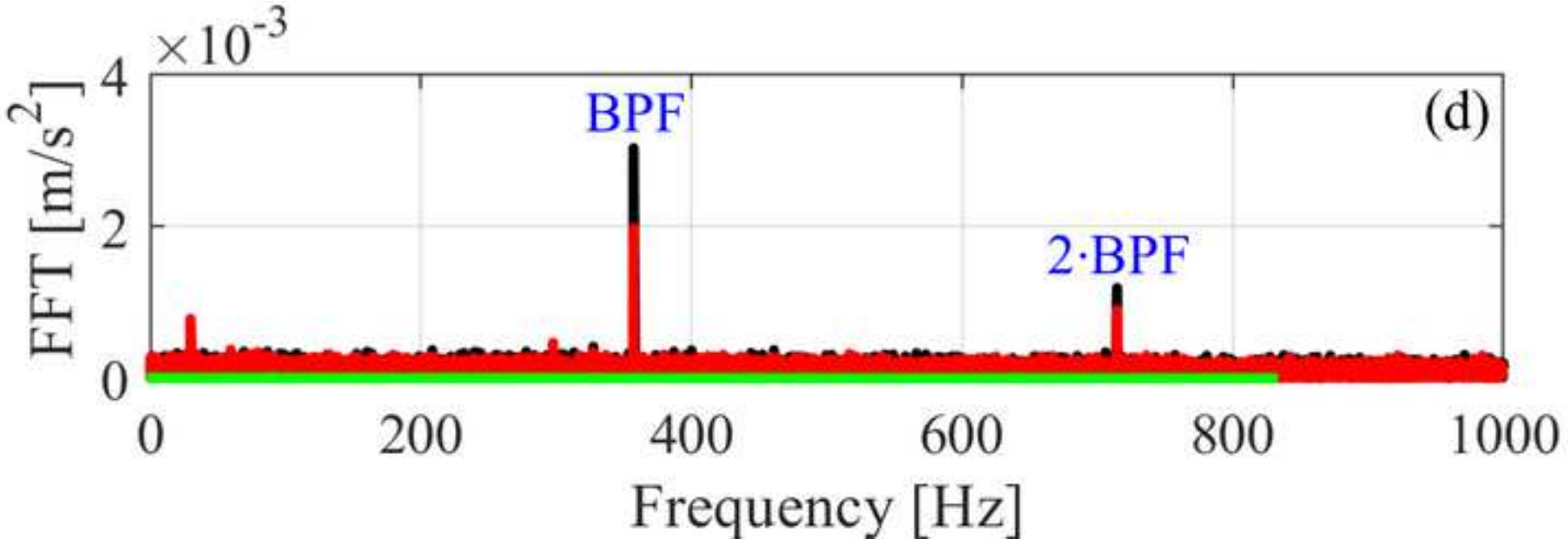

Declaration of interests

☒ The authors declare that they have no known competing financial interests or personal relationships that could have appeared to influence the work reported in this paper.

☐The authors declare the following financial interests/personal relationships which may be considered as potential competing interests:

We the undersigned agree with all of the above.

Author's name (Fist, Last)	Signature	Date
1. Georgios Mousmoulis		20/01/2021
2. Christos Yiakopoulos		20/01/2021
3. George Aggidis		20/01/2021
4. Ioannis Antoniadis	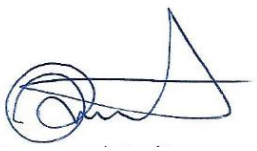	20/01/2021

5. Ioannis Anagnostopoulos  20/01/2021